

Article

## Monitoring of Evapotranspiration in a Semi-Arid Inland River Basin by Combining Microwave and Optical Remote Sensing Observations

Guangcheng Hu <sup>1</sup> and Li Jia <sup>1,2,\*</sup>

<sup>1</sup> State Key Laboratory of Remote Sensing Science, Institute of Remote Sensing and Digital Earth, Chinese Academy of Sciences, Beijing 100101, China; E-Mail: hugc@radi.ac.cn

<sup>2</sup> Joint Center for Global Change Studies (JCGCS), Beijing 100875, China

\* Author to whom correspondence should be addressed; E-Mail: jiali@radi.ac.cn; Tel.: +86-10-6480-7982; Fax: +86-10-6480-7982.

Academic Editors: George P. Petropoulos, Yoshio Inoue and Prasad S. Thenkabail

Received: 26 November 2014 / Accepted: 9 March 2015 / Published: 16 March 2015

**Abstract:** As a typical inland river basin, Heihe River basin has been experiencing severe water resource competition between different land cover types, especially in the middle stream and downstream areas. Terrestrial actual evapotranspiration (ET<sub>a</sub>), including evaporation from soil and water surfaces, evaporation of rainfall interception, transpiration of vegetation canopy and sublimation of snow and glaciers, is an important component of the water cycle in the Heihe River basin. We developed a hybrid remotely sensed ET<sub>a</sub> estimation model named ETMonitor to estimate the daily actual evapotranspiration of the Heihe River basin for the years 2009–2011 at a spatial resolution of 1 km. The model was forced by a variety of biophysical parameters derived from microwave and optical remote sensing observations. The estimated ET<sub>a</sub> was evaluated using eddy covariance (EC) flux observations at local scale and compared with the annual precipitation and the MODIS ET<sub>a</sub> product (MOD16) at regional scale. The spatial distribution and the seasonal variation of the estimated ET<sub>a</sub> were analyzed. The results indicate that the estimated ET<sub>a</sub> shows reasonable spatial and temporal patterns with respect to the diverse cold and arid landscapes in the upstream, middle stream and downstream regions, and is useful for various applications to improve the rational allocation of water resources in the Heihe River basin.

**Keywords:** evapotranspiration; validation; spatial and temporal variations; ETMonitor; Heihe River basin

## 1. Introduction

The Heihe River basin is the second largest inland river basin in northwest China, which is characterized by its distinct cold and arid landscapes. Water consumption has increased due to the increase of population and cropland in the middle reaches, resulting in a decrease of incoming water and a series of environmental problems in the lower reaches [1,2]. To allocate water to different water use units based on water requirements and equity, the Heihe River Basin Irrigation water resource management Decision Support System (HD) has been developed and validated in the Zhangye city of the Heihe River basin [3]. Terrestrial actual evapotranspiration (ETa), including evaporation from soil and water surfaces, evaporation of rainfall interception, transpiration of vegetation canopy and sublimation of snow and glaciers, is an important component of the water cycle in the Heihe River basin. Accurate estimates of ETa is needed to reduce uncertainties in constructing weekly to monthly water balances across catchments and regions, which require knowledge of distribution of ETa at daily scales [4]. To better understand the eco-hydrological processes across the Heihe River basin, in particular the water resource and water use in the upstream, middle stream and downstream regions and their interactions, it is essential to characterize accurately the spatial and temporal patterns of land surface evapotranspiration in a continuous and quasi-operational manner.

Among algorithms estimating terrestrial actual evapotranspiration at regional scale, those using land surface biophysical parameters derived from satellite remote sensing observations are very promising due to their capability of spatial coverage and yet frequent repeat in time. Widely used algorithms can be divided into four categories: simplified empirical regression methods [5,6], trapezoid or triangle feature space methods [7–9], surface energy balance based (single- and dual-source) models [10–14], and the traditional evapotranspiration estimation approaches, for instance the Penman–Monteith equation and Priestley–Taylor equation, combined with remote sensing [4,15–19]. Efforts have been made using different models mainly based on energy balance equation and taking the evapotranspiration as the residual on way or the other in combination with optical remote sensing, *i.e.*, using land surface temperature (LST) retrieved from thermal infrared bands as the main driving variable [20–22], of which some case studies were conducted in the Heihe River basin [9,23,24]. The main problem of the algorithms using LST is that the estimation approaches would be restricted to clear sky conditions. Besides, the physical meaning of the satellite-derived LST is unclear due to the mixed pixel problem, especially over heterogeneous and non-isothermal surfaces, and cannot be directly used as the aerodynamic temperature in estimating surface fluxes [25]. The estimated ETa as a residual of the energy balance contains biases from the net radiation, soil heat flux and sensible heat flux as well. Recently, some developments have been made based on the Soil–Vegetation–Atmosphere Transfer (SVAT) scheme, Penman–Monteith equation and remotely sensed data for the temporally and spatially continuous estimates of ETa, which is particularly useful for various applications since it is not limited to clear sky conditions [15–19,26].

The Penman–Monteith combination equation [27], which calculates evapotranspiration by combining the surface energy balance equation with other resistance-based methods, since it was proposed, has become a central component of very detailed evaporation equation incorporated in many land surface and atmospheric models [28,29]. The Shuttleworth–Wallace dual-source model [30] was proposed based on the Penman–Monteith equation for calculating soil evaporation and vegetation transpiration separately. The Shuttleworth–Wallace model is a biophysically sound framework for estimating terrestrial ET<sub>a</sub> at regional scale if the aerodynamic and surface resistances are well parameterized based on the remote sensing data and near-surface meteorological forcing data.

Considering the diverse landscapes and multi-climatic features in the Heihe River basin, and the demand of understanding the evapotranspiration processes for the whole river basin in different seasons, one should pay attention to the following issues: (1) The model should be robust enough to cover the processes of evaporation from bare soil and water surfaces, evaporation of rainfall interception, transpiration from grasses, crops and forests (perhaps also short vegetation understories beneath the forest canopy), sublimation of snow and glaciers. (2) Remote sensing data must be continuously available without gaps due to, for instance, clouds, instrument problems or other reasons. (3) Daily values of evapotranspiration are usually expected. In this study, we developed a hybrid remotely sensed ET<sub>a</sub> estimation model named ETMonitor to estimate the daily actual evapotranspiration of the Heihe River basin for the years 2009–2011 at a spatial resolution of 1 km. The estimation of soil evaporation and vegetation transpiration was based on the Shuttleworth–Wallace model with a variety of parameterization methods of the aerodynamic and bulk surface resistances, and the rainfall interception was estimated using a reformulated remote sensing based Gash model. The ETMonitor model uses a variety of biophysical parameters (except for LST) derived from microwave and optical remote sensing observations as input data to estimate the daily ET<sub>a</sub> for all sky conditions, which is particularly useful for routine applications in the Heihe River basin. The estimated ET<sub>a</sub> was evaluated using the *in-situ* observations and MODIS evapotranspiration product MOD16 at 3 eddy covariance (EC) flux sites located in the upstream and middle stream regions, and the spatial and temporal characteristics of ET<sub>a</sub> in the Heihe River basin were analyzed.

## 2. Study Area

The Heihe River basin is an inland river basin located in the arid region of northwest China, covering an area of approximately  $1.432 \times 10^5$  km<sup>2</sup> (Figure 1). The landscape of the basin is characterized by very different land cover types and different climate zones in upstream, middle stream and downstream regions:

(1) The upstream of the basin is a semi-humid, cold and high elevated mountainous region with the terrain elevation ranging from 2000 to 5000 m and the highest elevation of 5564 m above the sea level. The dominant land cover types are mountain forest (*Picea crassifolia*, *Sabina przewalskii*), alpine meadow, frozen soil, snow and glaciers. The annual precipitation is more than 350 mm/year and the mean annual air temperature is 1.5 °C–2.0 °C.

(2) The middle stream area of the Heihe River basin, with an elevation of 1300–1700 m, is characterized by typical irrigated artificial oasis and desert with semi-arid climate. The primary crops are maize, spring wheat, vegetables and small fraction of orchards. The annual precipitation in the middle reaches is 100–250 mm/yr and the mean annual air temperature is 2.8 °C–7.6 °C.

(3) The downstream area of the basin is well known as arid Gobi desert with an elevation of 900–1300 m. The vegetation cover mainly distributed as narrow strips (river greenbelt) along the river channel and a small oasis (named Ejin Banner Oasis) at the tail of the river. The dominant types of vegetation in the downstream region are *Populus euphratica*, *Tamarix chinensis*, and agricultural crops in the Ejin Oasis and along the river greenbelt. A terminal lake named East Juyanhai is located at the end of the river surrounded by desert. The annual precipitation in the downstream area is less than 50 mm/yr, and the mean annual air temperature is about 8.0 °C.

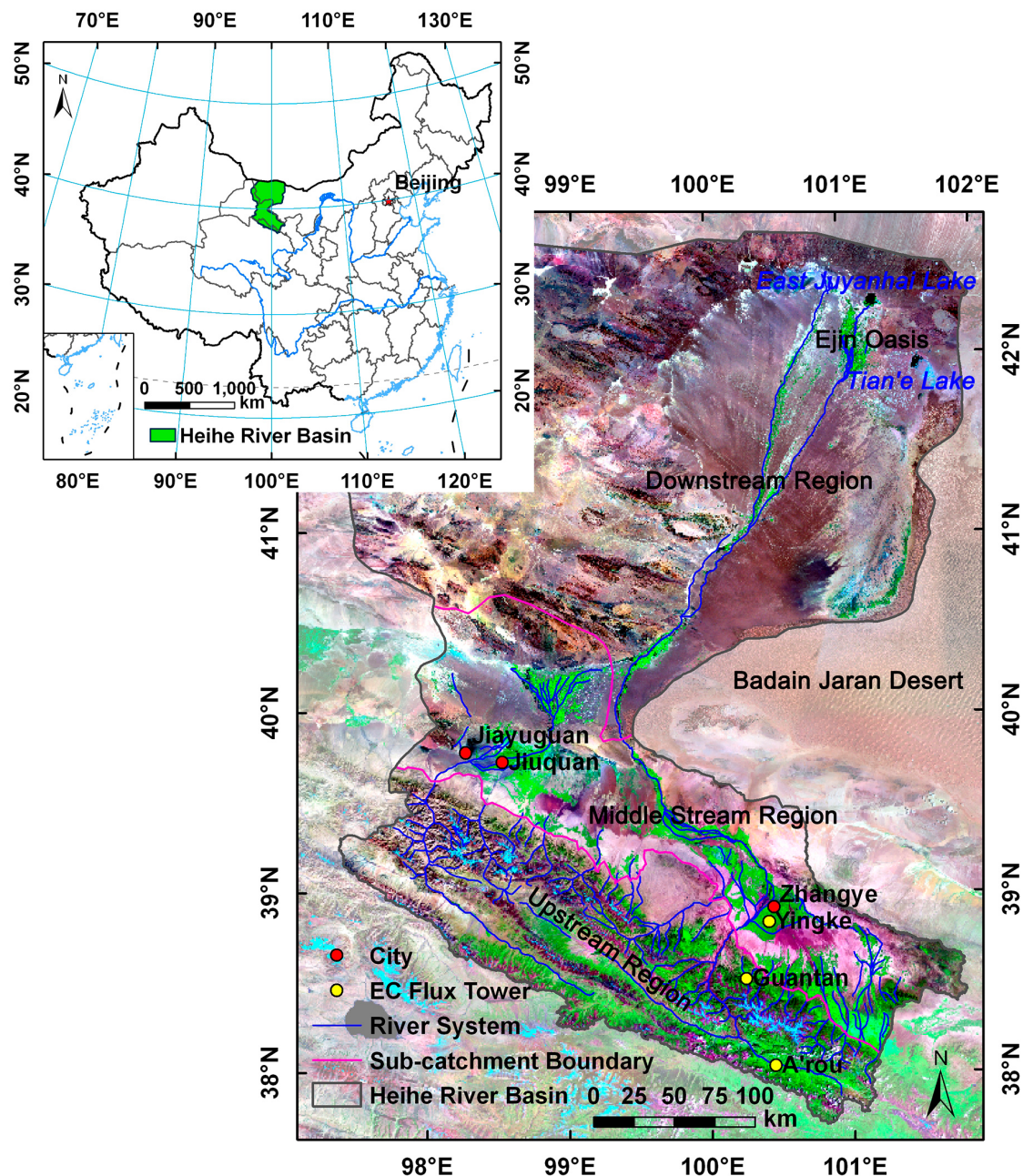


**Figure 1.** Locations of the Heihe River basin and the eddy covariance (EC) flux sites. The color composite remote sensing imagery of the landscape is mosaicked from Landsat-5 Thematic Mapper (TM) and Landsat-7 Enhanced Thematic Mapper Plus (ETM+) sensors (Red/band 7, Green/band 4, and Blue/band 2).

The water resource of the Heihe River is mainly from the rainfall, snow and glaciers in the upstream mountainous areas. Irrigation water used in the middle reaches agricultural area is mainly from the Heihe River through irrigation canals (main canal, branch canal, lateral canal, and field canal). Groundwater depletion is increasing year by year due to insufficient water supply from the river. Intensive use of water for crop irrigation in growing season over the middle reaches results in less or even cut-off of river water flow to the lower reaches every year. This, on one hand, influences the vegetation development in the downstream area, and on the other hand also perturbs the recharge of groundwater in the lower reaches. The ecosystem in the downstream area of the Heihe River basin is therefore under vulnerable conditions.

### 3. Theoretical Formulation of the ETMonitor Model

The ETMonitor model combines different ETa parameterizations for the following land cover types (Figure 2): (1) water body; (2) snow/ice surface; and (3) soil–vegetation canopy. For different vegetation types, the evaporation of rainfall interception is also taken into account in ETMonitor. The theoretical formulation of the ETMonitor will be presented in this section, and the forcing data will be briefly introduced in Section 4.

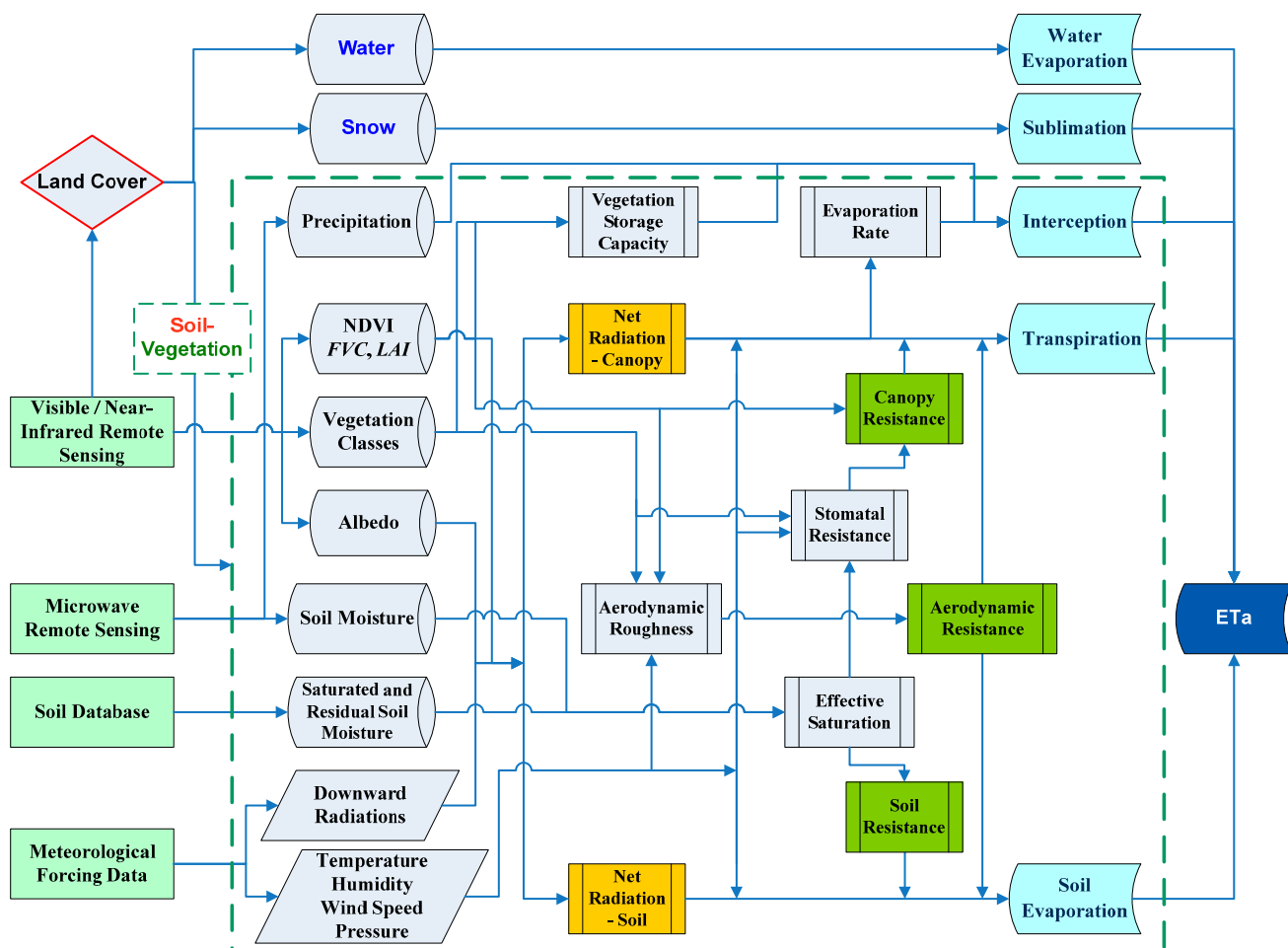


**Figure 2.** Flowchart of the ETMonitor model combining different evapotranspiration (ET<sub>a</sub>) parameterizations.

### 3.1. Evapotranspiration of the Soil–Vegetation Unity

#### 3.1.1. Shuttleworth–Wallace Dual-Source Model

For an incomplete (partial) soil–vegetation canopy, the model is constructed with a dual-source scheme that distinguishes the energy partitioning and water fluxes between soil and vegetation (*i.e.*, evaporation from the soil and transpiration from the vegetation canopy). The model structure together with its resistance scheme is illustrated in Figure 3.

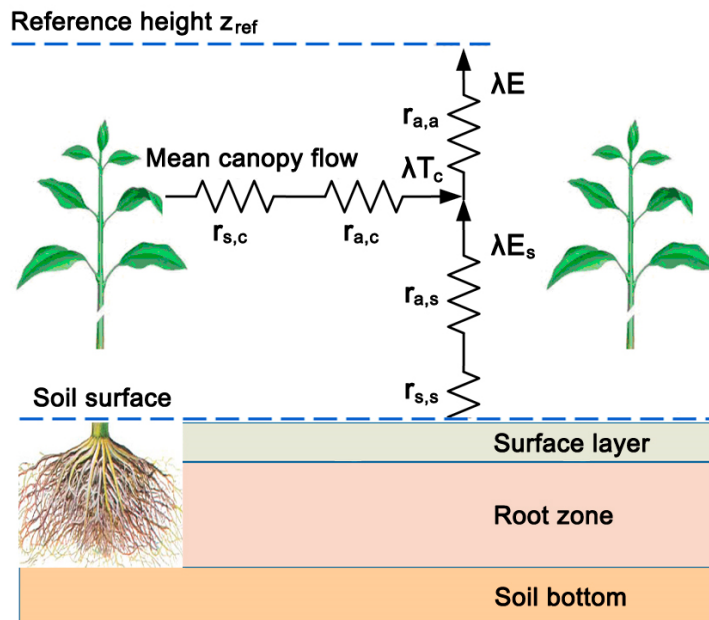


**Figure 3.** Schematic description of the latent heat flux partitioning with the relevant resistances for partial soil–vegetation canopy used in ETMonitor.

The Shuttleworth–Wallace dual-source model [30] is adopted to account separately for the energy balance for vegetation and soil components of a soil–vegetation canopy unity. Assuming aerodynamic mixing occurring at a mean canopy source height within the canopy, a variant form of Penman–Monteith equation that combines energy balance with plant physiology and soil water diffusion can be written for  $\lambda E$ :

$$\lambda E = C_c \cdot PM_c + C_s \cdot PM_s \quad (1)$$

$$PM_c = \frac{\Delta(R_n - G) + [\rho C_p VPD - \Delta r_{a,c} (R_{n,s} - G)] / (r_{a,a} + r_{a,c})}{\Delta + \gamma[1 + r_{s,c} / (r_{a,a} + r_{a,c})]} \quad (2)$$

$$PM_s = \frac{\Delta(R_n - G) + (\rho C_p VPD - \Delta r_{a,s} R_{n,c}) / (r_{a,a} + r_{a,s})}{\Delta + \gamma[1 + r_{s,s} / (r_{a,a} + r_{a,s})]} \quad (3)$$

$$C_c = \{1 + R_c \cdot R_a / [R_s \cdot (R_c + R_a)]\}^{-1} \quad (4)$$

$$C_s = \{1 + R_s \cdot R_a / [R_c \cdot (R_s + R_a)]\}^{-1} \quad (5)$$

$$R_a = (\Delta + \gamma) \cdot r_{a,a} \quad (6)$$

$$R_s = (\Delta + \gamma) \cdot r_{a,s} + \gamma \cdot r_{s,s} \quad (7)$$

$$R_c = (\Delta + \gamma) \cdot r_{a,c} + \gamma \cdot r_{s,c} \quad (8)$$

where  $\lambda E$  ( $\text{W}\cdot\text{m}^{-2}$ ) is the bulk latent heat flux of the soil–vegetation unity and  $\lambda$  ( $\text{J}\cdot\text{kg}^{-1}$ ) is the latent heat of evaporation.  $PM_c$  and  $PM_s$  ( $\text{W}\cdot\text{m}^{-2}$ ) are variables related to canopy transpiration and soil evaporation,  $C_c$  and  $C_s$  (dimensionless) are the surface resistance coefficients for canopy and soil, respectively.  $G$  ( $\text{W}\cdot\text{m}^{-2}$ ) is the conductive heat flux from soil surface to deeper soil layer,  $R_n$  ( $\text{W}\cdot\text{m}^{-2}$ ) is the total net radiation flux,  $R_{n,c}$  and  $R_{n,s}$  ( $\text{W}\cdot\text{m}^{-2}$ ) are net radiation flux absorbed by the vegetation canopy and arrives at the soil surface, respectively, which can be estimated based on the remotely sensed albedo and fractional vegetation cover (FVC).  $\Delta = d(e_{\text{sat}})/dT \cdot (\text{Pa}\cdot\text{K}^{-1})$ , which is the slope of the curve relating saturated water vapor pressure  $e_{\text{sat}}$  (Pa) to temperature  $T$  (K),  $\rho$  ( $\text{kg}\cdot\text{m}^{-3}$ ) is the air density,  $C_p$  ( $\text{J}\cdot\text{kg}^{-1}\cdot\text{K}^{-1}$ ) is the specific heat of air,  $\gamma \cdot (\text{Pa}\cdot\text{K}^{-1})$  is the psychrometric constant,  $VPD$  (Pa) is the vapor pressure deficit of the air at the reference height above the canopy. The terms  $R_a$ ,  $R_s$ , and  $R_c$  ( $\text{Pa K}^{-1}\cdot\text{s}\cdot\text{m}^{-1}$ ) are the total aerodynamic resistances to vapor transport for the whole soil–vegetation canopy, the soil and the vegetation, respectively, that are derived from the surface resistance and aerodynamic resistance.  $r_{a,c}$  ( $\text{s}\cdot\text{m}^{-1}$ ) is the boundary layer aerodynamic resistance between the canopy and the canopy source height,  $r_{s,c}$  ( $\text{s}\cdot\text{m}^{-1}$ ) is the bulk canopy surface resistance,  $r_{a,s}$  ( $\text{s}\cdot\text{m}^{-1}$ ) is the aerodynamic resistance between the soil surface and the canopy source height,  $r_{s,s}$  ( $\text{s}\cdot\text{m}^{-1}$ ) is the soil surface resistance. The  $r_{a,a}$  ( $\text{s}\cdot\text{m}^{-1}$ ) illustrated in Figure 3 is the aerodynamic resistance between the canopy source height and the reference height above the canopy. The canopy source height is taken at  $d + z_{0m}$  (m), where  $d$  (m) and  $z_{0m}$  (m) are zero plane displacement height and aerodynamic roughness length for momentum transfer of the soil–vegetation canopy, respectively.

### 3.1.2. Resistances

There have been numerous studies and achievements on parameterization methods of the above resistances since the 1970s based on field experiments and modeling at field scale over different vegetation and soil management regimes. ETMonitor adopts resistance equations and corresponding parameters from previous studies for different landscapes, which are described below together with the relevant literatures.

#### (1) Aerodynamic Resistance

Three aerodynamic resistances, *i.e.*,  $r_{a,a}$ ,  $r_{a,c}$ , and  $r_{a,s}$  ( $\text{s}\cdot\text{m}^{-1}$ ), used in the ETMonitor model (as shown in Figure 3) are taken from [31]:

$$r_{a,a} = \frac{u_{\text{zref}} - u_c}{u_{\text{zref}}} r_a \quad (9)$$

$$r_{a,c} = \frac{u_c}{\sigma_a u_{\text{zref}}} r_a \quad (10)$$

$$r_{a,s} = \frac{u_c}{(1 - \sigma_a) u_{\text{zref}}} r_a \quad (11)$$

where  $u_{z\text{ref}}$  ( $\text{m}\cdot\text{s}^{-1}$ ) is the wind speed at the reference height  $z_{\text{ref}}$  (m) above the canopy,  $u_c$  ( $\text{m}\cdot\text{s}^{-1}$ ) is the wind speed at the canopy source height ( $d + z_{0\text{m}}$ ) (m),  $r_a$  ( $\text{s}\cdot\text{m}^{-1}$ ) is the overall aerodynamic resistance for momentum transfer in the soil–vegetation unity:

$$r_a = \frac{1}{k^2 u_{z\text{ref}}} \left[ \ln\left(\frac{z_{\text{ref}} - d}{z_{0\text{m}}}\right) - \Psi_m \right] \left[ \ln\left(\frac{z_{\text{ref}} - d}{z_{0\text{h}}}\right) - \Psi_h \right] \quad (12)$$

where  $k$  is von Karman coefficient (0.41),  $\psi_m$  and  $\psi_h$  are stability correction functions (neutral condition is assumed at daily step of calculation so as  $\psi_m = 0$  and  $\psi_h = 0$ ). The roughness length for heat transfer  $z_{0\text{h}}$  (m) is set as  $0.1z_{0\text{m}}$  (m).

In Equations (10) and (11)  $\sigma_a$  is a momentum partition coefficient (*i.e.*, momentum absorption is assumed to take place partly by the canopy and partly by the soil) assumed to be a function of Leaf Area Index (LAI) [32] and given by:

$$\sigma_a = 1 - \frac{0.5}{0.5 + LAI} \exp\left(-\frac{LAI^2}{8}\right) \quad (13)$$

The  $u_c$  ( $\text{m}\cdot\text{s}^{-1}$ ) in Equations (9)–(11) is parameterized as:

$$u_c = 0.83\sigma_f u_{z\text{ref}} + (1 - \sigma_f)u_{z\text{ref}} \quad (14)$$

where  $\sigma_f$  is an extinction coefficient, ranging between 0 (for bare soil) and 1 (for full vegetation cover) [33]. In ETMonitor,  $\sigma_f$  is taken as the same value as  $\sigma_a$ , which depends on LAI and covers the same range of values, satisfying the gradual transition from bare soil to a closed canopy [31].

## (2) Soil Surface Resistance

Following Camillo *et al.*, Clapp *et al.* and Dolman [34–36], the soil surface resistance to vapor flux  $r_{s,s}$  ( $\text{s}\cdot\text{m}^{-1}$ ) is parameterized as a function of minimum soil surface resistance (under optimal water condition)  $r_{s,s,\text{min}}$  ( $\text{s}\cdot\text{m}^{-1}$ ) and relative water content of soil surface layer  $\theta_g'$  (dimensionless):

$$r_{s,s} = r_{s,s,\text{min}} (\theta_g')^{-3} \quad (15)$$

where  $r_{s,s,\text{min}}$  is taken as  $50 \text{ s}\cdot\text{m}^{-1}$ . The relative water content of soil surface layer  $\theta_g'$  is calculated as a degree of saturation of the surface layer volumetric soil water content  $\theta_g$  ( $\text{cm}^3\cdot\text{cm}^{-3}$ ) [37] derived from the observations by the passive microwave radiometer, *i.e.*, the Advanced Microwave Scanning Radiometer–Earth Observing System (AMSR-E):

$$\theta_g' = \frac{\theta_g - \theta_{\text{res}}}{\theta_{\text{sat}} - \theta_{\text{res}}} \quad (16)$$

where  $\theta_{\text{sat}}$  and  $\theta_{\text{res}}$  ( $\text{cm}^3\cdot\text{cm}^{-3}$ ) are saturated and residual soil water contents which are soil types dependent.

## (3) Canopy Surface Resistance

The canopy surface resistance is estimated by scaling up leaf stomatal resistance with canopy leaf area. The stomatal resistance  $r_{st}$  ( $\text{s}\cdot\text{m}^{-1}$ ) depends on ambient factors (available energy and atmospheric water demand) and available soil moisture in the root zone. Taking  $r_{st,\text{min}}$  ( $\text{s}\cdot\text{m}^{-1}$ ) as the minimum stomatal resistance (defined as the value of stomatal resistance under fully open stomata conditions

with sufficient energy and water supply), the canopy surface resistance  $r_{s,c}$  ( $\text{s} \cdot \text{m}^{-1}$ ) is parameterized by a multiplicative response to several environmental factors [38–40],

$$r_{s,c} = \frac{F_s}{LAI} \frac{r_{st,min}}{f_1(R_s)f_2(T_a)f_3(VPD)f_4(\theta_r)} \quad (17)$$

where  $LAI$  ( $\text{m}^2 \cdot \text{m}^{-2}$ ) is the leaf area index,  $F_s$  is the leaf shadowing factor and a function of  $LAI$  and canopy structure,  $f_1(R_s)$ ,  $f_2(T_a)$ ,  $f_3(VPD)$  and  $f_4(\theta_r)$  are functions (limiting factors) that describes stomatal response to environmental factors of solar radiation  $R_s$  ( $\text{W} \cdot \text{m}^{-2}$ ), air temperature  $T_a$  ( $^\circ\text{C}$ ), vapour pressure deficit  $VPD$  (hPa) and root zone soil water content  $\theta_r$  ( $\text{cm}^3 \cdot \text{cm}^{-3}$ ), respectively.

Following Mehrez *et al.* [41] the leaf shadowing factor  $F_s$  is linked to  $LAI$  by:

$$F_s = 0.3LAI + 1.2 \quad (18)$$

The limiting factors  $f_i(variables)$  ( $i = 1, 2, 3, 4$ ) are adopted from literatures [40,42–45] and given below:

$$f_1(R_s) = 1 - \exp(-\frac{R_s}{k_{Rs}}) \quad (19)$$

$$f_2(T_a) = \frac{(T_a - T_L)(T_H - T_a)^a}{(T_{opt} - T_L)(T_H - T_{opt})^a} \quad (20)$$

$$a = \frac{T_H - T_{opt}}{T_{opt} - T_L} \quad (21)$$

$$f_3(VPD) = 1 - k_{VPD} VPD \quad (22)$$

where  $k_{Rs}$  is taken as  $500 \text{ W} \cdot \text{m}^{-2}$ ,  $k_{VPD}$ ,  $T_L$ ,  $T_{opt}$  and  $T_H$  depends on vegetation types. For  $k_{VPD}$ , Noilhan *et al.* [46] has derived a value of  $0.025 \text{ hPa}^{-1}$  for a coniferous forest, Stewart [40] has obtained a value of  $0.0155 \text{ hPa}^{-1}$  for rainfed grass prairie, and a value of  $0.023 \text{ hPa}^{-1}$  is taken for crops in ETMonitor.  $T_L$ ,  $T_{opt}$  and  $T_H$  are the lower, optimum and upper air temperature limits of stomatal activity, which can be taken as  $5 \text{ }^\circ\text{C}$ ,  $35 \text{ }^\circ\text{C}$  and  $55 \text{ }^\circ\text{C}$  for maize (C<sub>4</sub> carbon fixation),  $0 \text{ }^\circ\text{C}$ ,  $25 \text{ }^\circ\text{C}$  and  $50 \text{ }^\circ\text{C}$  for the other crop varieties and grasses (C<sub>3</sub> carbon fixation),  $0 \text{ }^\circ\text{C}$ ,  $20 \text{ }^\circ\text{C}$  and  $40 \text{ }^\circ\text{C}$  for the forests, respectively.

A sinusoidal function is used to take into account the influence of root zone soil moisture deficit on the stomatal closure [15,47],

$$f_4(\theta_r) = K_{sf} \theta_r - \frac{\sin(2\pi\theta_r')}{2\pi} \quad (23)$$

$$\theta_r' = 0.1LAI + (1 - 0.1LAI) \{1 - \exp[\theta_g'(-0.5LAI - 1)]\} \quad (24)$$

where  $\theta_r'$  (dimensionless) is the relative water content of the root zone. The parameter  $K_{sf}$  is a tenacity factor that describes the ability of plants to extract soil moisture and ranges from 1 for drought sensitive plants to 1.5 for moderately drought sensitive plants and to 3 for insensitive plants.

The limiting factors  $f_i(variables)$  have values between 0 and 1 (0 for full closure of stomata which leads to infinite resistance; 1 for fully open stomata which leads to minimum stomatal resistance corresponding to optimum conditions). When all environmental conditions are under optimum, all the  $f_i(variables)$  are equal to unity and the stomatal resistance  $r_{st}$  takes the minimum value of  $r_{st,min}$ . Under conditions away from the optimum, the stomatal resistance is increased from its minimum value  $r_{st,min}$ .

When one or more of the  $f_i(variables)$  reach zero, Equation (17) becomes infinite resistance value, in this case a maximum value of  $5 \times 10^4 \text{ s} \cdot \text{m}^{-1}$  is given to  $r_{s,c}$ .

### 3.2. Interception

Interception is the rainfall intercepted by the vegetation canopy and subsequently evaporated back to the atmosphere. We estimated the interception of different vegetation types in the Heihe River basin using a reformulated Gash analytical model [48,49] called RS–Gash model (remote sensing based Gash model). The reformulated Gash model is forced by remote sensing observations of canopy structure (e.g., FVC, LAI, vegetation storage capacity) and rainfall intensity [50,51]. The interception of canopy and trunk was replaced by the interception of vegetation, and the sub-pixel heterogeneity was taken into account by applying a Poisson distribution function to the LAI value of each pixel. The detailed model description and validation is given in parallel work by Cui and Jia [50] and Cui *et al.* [51].

### 3.3. Sublimation

Sublimation of snow and ice (glaciers) occurs more readily when the near-surface water vapor pressure is less than the saturated water vapor pressure. The sublimation of snow and ice was estimated using the formula developed by Kuzmin [52] and recommended for application by the World Meteorological Organization (WMO):

$$E_{\text{ice}} = (0.18 + 0.098u_{10})(e_s - e_2) \quad (25)$$

where  $E_{\text{ice}}$  ( $\text{mm} \cdot \text{d}^{-1}$ ) is the sublimation of snow and ice,  $u_{10}$  ( $\text{m} \cdot \text{s}^{-1}$ ) is the wind speed at a height of 10 m above the surface,  $e_2$  (hPa) is the actual water vapor pressure at a height of 2 m,  $e_s$  (hPa) is the saturated water vapor pressure.

### 3.4. Evaporation from Water Surface

The classical Penman equation [53] was used to estimate the evaporation from water surface:

$$\lambda E_{\text{water}} = \frac{\Delta(R_n - G) + \gamma E_a}{\Delta + \gamma} \quad (26)$$

$$E_a = 6.43(a_w + b_w u_2)(e_s - e_2) \quad (27)$$

where  $\lambda E_{\text{water}}$  is the latent heat of evaporation in  $\text{MJ} \cdot \text{m}^{-2} \cdot \text{day}^{-1}$ ,  $\lambda$  is as defined in Equation (1) in  $\text{MJ} \cdot \text{kg}^{-1}$ ,  $R_n$  and  $G$  are as defined in Equation (2) in  $\text{MJ} \cdot \text{m}^{-2} \cdot \text{day}^{-1}$ ,  $\Delta$  and  $\gamma$  are as defined in Equation (2) in  $\text{kPa} \cdot \text{K}^{-1}$ ,  $e_2$  and  $e_s$  are as defined in Equation (25) in kPa.  $u_2$  ( $\text{m} \cdot \text{s}^{-1}$ ) is the wind speed at a height of 2 m,  $a_w$  and  $b_w$  are wind function coefficients, which are taken as 0.5 and 0.54 for open water.

## 4. Data

### 4.1. Remote Sensing Data

In the ETMonitor model, the biophysical variables derived from microwave and optical remote sensing observations include albedo, FVC, LAI, surface layer volumetric soil water content  $\theta_g$ , and land cover types, which are described separately in this section.

#### 4.1.1. Land Surface Albedo

Land surface albedo is a critical variable affecting the radiative energy budget and the convective overturning. The albedo data used in this study is the Global LAnd Surface Satellite (GLASS) albedo product from 2009 to 2011, which is produced at 1 km spatial resolution and in eight-day steps in the Sinusoidal projection [54]. The GLASS albedo product is a gapless and long-term continuous data set with an accuracy similar to that of the Moderate Resolution Imaging Spectroradiometer (MODIS) MCD43 product.

#### 4.1.2. Normalized Difference Vegetation Index (NDVI)

The NDVI was used to indicate the vegetation conditions and to calculate the FVC [33] and LAI [15]. The NDVI data used in this study is MODIS vegetation index (VI) product MOD13A2 (1-km/16-day) from 2009 to 2011 in the Sinusoidal projection. Cloud presence usually contaminates remotely sensed data, especially for the optical and thermal infrared bands. MODIS NDVI data is provided at 16-day compositing periods utilizing three compositing schemes to reduce the artifacts due to clouds and aerosols. For some time periods that cloud cover can persist longer than the compositing period; these compositing schemes cannot eliminate atmospheric contamination. Therefore a time series reconstruction algorithm proposed by Jia *et al.* [55] based on the Harmonic Analysis of Time Series (HANTS) approach and the Temporal–Similarity–Statistics (TSS) method was implemented to obtain daily cloud-free NDVI time series being consistent at spatial and temporal scales.

#### 4.1.3. Soil Moisture

Soil moisture is a key variable in understanding land surface hydrology and controls the ecological, hydrometeorological and biogeochemical processes. Land surface soil moisture was derived from the passive microwave radiometer AMSR-E on the Aqua satellite. Daily surface soil moisture product at 25 km spatial resolution was obtained from the National Snow and Ice Data Center (NSIDC). The daily soil moisture for every four days were averaged to obtain four-day aggregated soil moisture and then downscaled to 1 km using the bilinear resampling method.

#### 4.1.4. Land Cover

Land cover type is a crucial parameter that is required for creating look-up tables about certain biophysical properties, such as the minimum stomatal resistance and the optimal air temperature for the growth of the plant. The Multi-source Integrated Chinese Land Cover (MICLCover) data at 1 km spatial resolution used in this study was generated by combining multi-source Land Use/Land Cover (LULC) products based on the Dempster–Shafer evidence theory [56]. The land cover scheme identifies 17 land cover types defined by the International Geosphere–Biosphere Programme (IGBP). The crop varieties (maize, spring wheat, and potato) were also accounted for using the land cover map provided by the Heihe Plan Science Data Center [57]. The water, permanent snow and glaciers mask was derived from the MODIS land cover type product MCD12Q1 from 2009 to 2011 to indicate the yearly dynamics of surface water, snow and glaciers.

#### 4.1.5. Snow Cover Extent

Snow cover plays a significant role in land surface models and hydrometeorology studies. In this study, the MODIS remotely sensed snow cover extent product was used as model input, *i.e.*, the maximum snow cover extent over an eight-day compositing period at 500 m spatial resolution derived from the MODIS/Terra Snow Cover (MOD10A2) data set. The MODIS snow cover data is derived using a snow-mapping algorithm based on the Normalized Difference Snow Index (NDSI) and other criteria tests for snow reflectance characteristics in the visible and near-infrared regions.

#### 4.1.6. Precipitation

The version 7 of Tropical Rainfall Measuring Mission (TRMM) Multi-satellite Precipitation Analysis (TMPA) product 3B42V7 was used to estimate the interception. The 3B42V7 with the spatial and temporal resolutions of 0.25°/tri-hourly over 50°N–50°S is available from 1998 to present. The daily precipitation was obtained by summing up all of the corresponding tri-hourly values for each day, and then spatially interpolated onto the MODIS grid using a bilinear interpolation algorithm.

### 4.2. Soil Texture and Hydraulic Parameters

The saturated and residual soil water contents of soil surface layer were provided by the China dataset of soil hydraulic parameters [58]. The dataset is derived from multi-PTFs (Pedotranfer Functions), including the parameters in the Clapp and Hornberger Functions (FCH) and in the van Genuchten and Mualem Functions (FGM), respectively. It is available at 30 arc-second (1 km) and seven vertical layers to the depth of 1.38 m.

### 4.3. Meteorological Forcing Data

The near-surface meteorological forcing data, including air temperature, air pressure, specific humidity, wind speed, downward short-wave and long-wave radiation fluxes are essential to drive the ETMonitor. The 5 km/1 h meteorological forcing data from 2009 to 2011 over the Heihe River basin used in this study was derived based on the Weather Research and Forecasting model (WRF) simulation [59,60].

The 5 km/1 h meteorological forcing data was statistically downscaled to the spatial–temporal resolution of 1 km/daily. First, the hourly data was averaged to daily for every meteorological parameter. Second, the spatial resolution of 5 km was downscaled to 1 km using statistical downscaling approaches for daily air temperature, air pressure, specific humidity, downward short-wave and long-wave radiations. The statistical downscaling is based on the semi-empirical relationships and on the multiple predictor variables (topographic altitude, aspect, and slope, at 1 km and 5 km spatial resolutions) and transfer functions [61,62]. Then the wind speed was downscaled to 1 km using the bilinear resampling method.

### 4.4. Eddy Covariance Flux Data

The estimated ET<sub>a</sub> by ETMonitor was evaluated using the ground measurements across different ecosystems at three eddy covariance flux sites in 2009–2011. The latter were collected from the Watershed Allied Telemetry Experimental Research (WATER) and provided by the Cold and Arid

Regions Sciences Data Center at Lanzhou (available at <http://westdc.westgis.ac.cn/> (accessed on 1 November 2014)) [63–65]. The ground measurements of latent heat flux with a time interval of 30-minute by the eddy covariance method at the towers were measured and processed. The 30-minute flux data were obtained from the raw data sampled at 10 Hz using the post-processing software EdiRe, and then the half-hourly results were screened following the criteria proposed by Blanken *et al.* [66]. The quality controlled 30-minute latent heat flux was then aggregated to daily and eight-day values for comparison with the estimated ET<sub>a</sub> at consistent temporal intervals.

The three EC flux sites include Yingke, A'rou and Guantan, representing different climate and land cover types in the Heihe River basin (Table 1). The Yingke site is located in the middle reaches of the basin, and the other two sites are located in the upper reaches (Figure 1). The source areas of the EC measurements were within a radius of 250 m at these three sites [65]. The Energy Balance Ratio (EBR), *i.e.*, the ratio of the turbulent energy fluxes (the sum of sensible and latent heat fluxes) to the available energy (net radiation flux minus soil surface heat flux) was used to indicate the energy balance closure at these three EC sites [65], and the values were similar to that (approximately 70%–90%) previously observed for cropland, grassland and forest sites [67–69].

**Table 1.** Eddy covariance flux sites of the Watershed Allied Telemetry Experimental Research (WATER) used for ET<sub>a</sub> evaluation at local scale.

Site Name	Sensors	Location/Elevation	Landscape	Data DOI
Yingke	CSAT3 (Campbell) and Li7500 (Li-cor)	100°24'37.2"E	Cropland (maize)	10.3972/water973.0278.db
		38°51'25.7"N 1519.1 m		
		100°27'52.9"E 38°02'39.8"N 3032.8 m		
Guantan		100°15'00.8"E 38°32'01.3"N 2835.2 m	Spruce Forest	10.3972/water973.0294.db

#### 4.5. MOD16 ET<sub>a</sub>

We also compared the estimated ET<sub>a</sub> by ETMonitor with the MODIS global evapotranspiration product MOD16, which is the first published 1 km ET<sub>a</sub> data set for the global vegetated land areas at eight-day, monthly and annual intervals [18,19] partly driven by remote sensing data. In the MOD16 product, the calculation of ET<sub>a</sub> were not made over non-vegetated pixels, *i.e.*, water body, barren or sparsely vegetated, permanent snow and ice, permanent wetland and urban areas, but assigned by filled values. The data used for the comparative study is the MOD16A2 ET<sub>a</sub> product, which is produced at 1 km spatial resolution and eight-day compositing periods (mm/8-day) in the Sinusoidal projection.

## 5. Results

### 5.1. Validation of the Model

#### 5.1.1. Comparison with the Ground Measurements

Three-year (2009–2011) time series of daily latent heat flux  $\lambda E$  ( $\text{W/m}^2$ , or ET<sub>a</sub> when expressed in  $\text{mm/day}$ ) of the Heihe River basin was derived by the ETMonitor model. In order to evaluate the accuracy of the ETMonitor model, the estimated daily  $\lambda E$  was compared with the EC observations at the site of Yingke (cropland), A'rou (alpine meadow), and Guantan (forest) separately (Figure 4). For such comparison, one should keep in mind that the estimated pixel values of  $\lambda E$  might be different from *in-situ* measurements for the obvious spatial scale difference between the ground measurements and the satellite pixels [70–72]. The source areas of the EC measurements were within a radius of 250 m at these three sites [65]. ETMonitor performs the best at A'rou, then followed at Yingke with the coefficient of determination ( $R^2$ , the square of the correlation coefficient between ETMonitor and EC measurements) higher than 0.8. At Guantan, the discrepancy between estimated  $\lambda E$  and EC observations is relatively large with the  $R^2$  of 0.7. The root mean square error (RMSE) at the Yingke site is  $24.8 \text{ W/m}^2$ , a little higher than that of the other two sites.

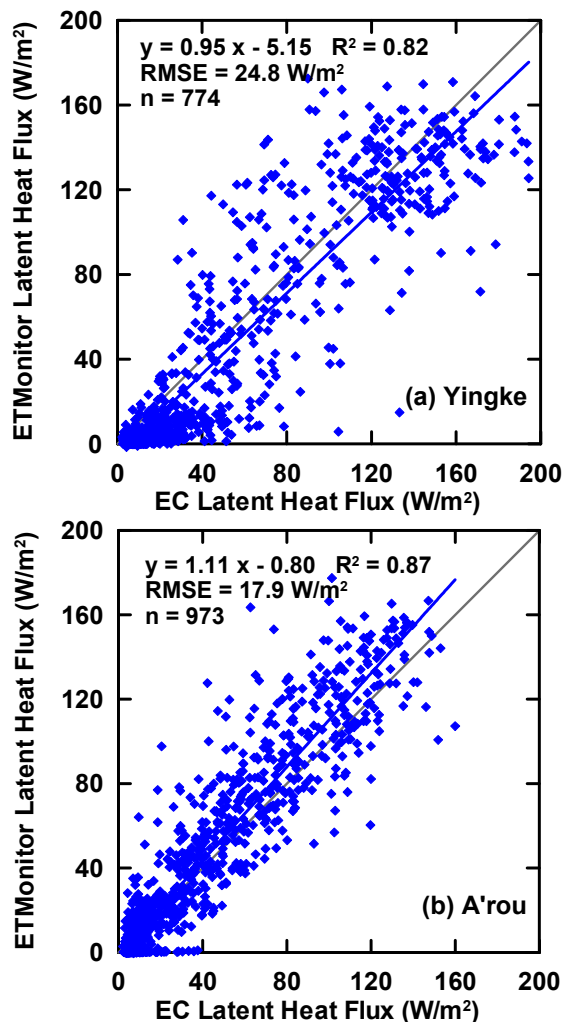


**Figure 4. Cont.**

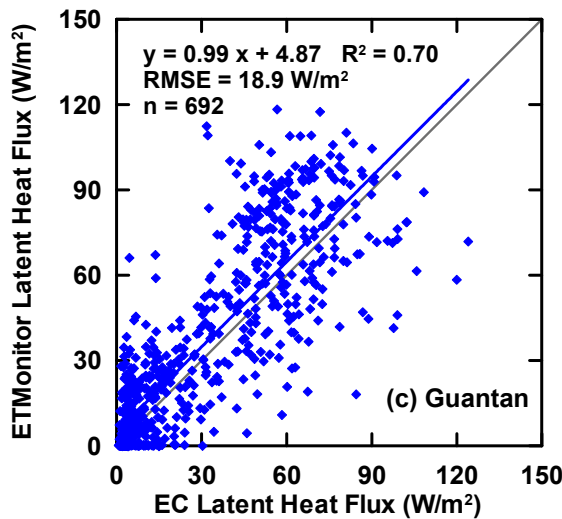


**Figure 4.** Scattering plots of the ETMonitor latent heat flux ( $\lambda E$ ) against eddy covariance (EC) observations spanning 2009–2011 at the site of (a) Yingke (cropland), (b) A’rou (alpine meadow), and (c) Guantan (forest). Values shown are the daily values of latent heat flux,  $\lambda E$  ( $\text{W}/\text{m}^2$ ).

We additionally compared the ETMonitor output with the MOD16 ETa at these three EC sites. The estimated daily ETa was aggregated to eight-day means and the time series plots and scatter plots at each site are shown in Figures 5 and 6 to provide the assessment of the seasonal performance and statistical results of ETMonitor and MOD16 ETa. At the Guantan site, the missing EC data for most of 2009 was due to the deficiency of solar power, instrument malfunction, poor maintenance, and bad weather conditions (Figure 5c). In general, fairly good results have been obtained from this validation, showing that the ETMonitor model can reproduce the time series of ETa observed at local scale to some degree for these three landscapes. At Yingke in the spring season, the ETMonitor ETa was obviously underestimated due to the underestimated surface layer soil moisture (Figure 5a). The cropland in the oasis was irrigated in late autumn of the previous year, and then the water was stored in the frozen soil. In spring, the liquid soil water content is very high during thawing of frozen soil, enhancing the process of soil evaporation. However, such a damped process was not captured by the AMSR-E soil moisture data used in this study. On one hand the AMSR-E soil moisture with rather coarse spatial resolution is a mixing contribution from different land surface elements, which may have smoothed out the spatial variability in land surface soil moisture. On the other hand, other studies have revealed that the AMSR-E soil moisture product exhibits underestimates [73,74]. The MOD16 ETa is overestimated in winter, whereas in the growing season, it is much lower than EC observations at these three sites, especially at the Yingke Oasis station (Figure 5a). In general, the ETMonitor estimated ETa is closer to the EC observations than MOD16 with better correlation, smaller RMSE between ETMonitor and EC measurements. The  $R^2$  of ETMonitor vs. EC (MOD16 vs. EC) is 0.92 (0.64), 0.96 (0.71), 0.87 (0.41) and the RMSE of ETMonitor vs. EC (MOD16 vs. EC) is 0.59 (1.74) mm/day, 0.39 (0.83) mm/day, 0.39 (0.70) mm/day at the site of Yingke, A’rou, and Guantan, respectively (Figure 6).

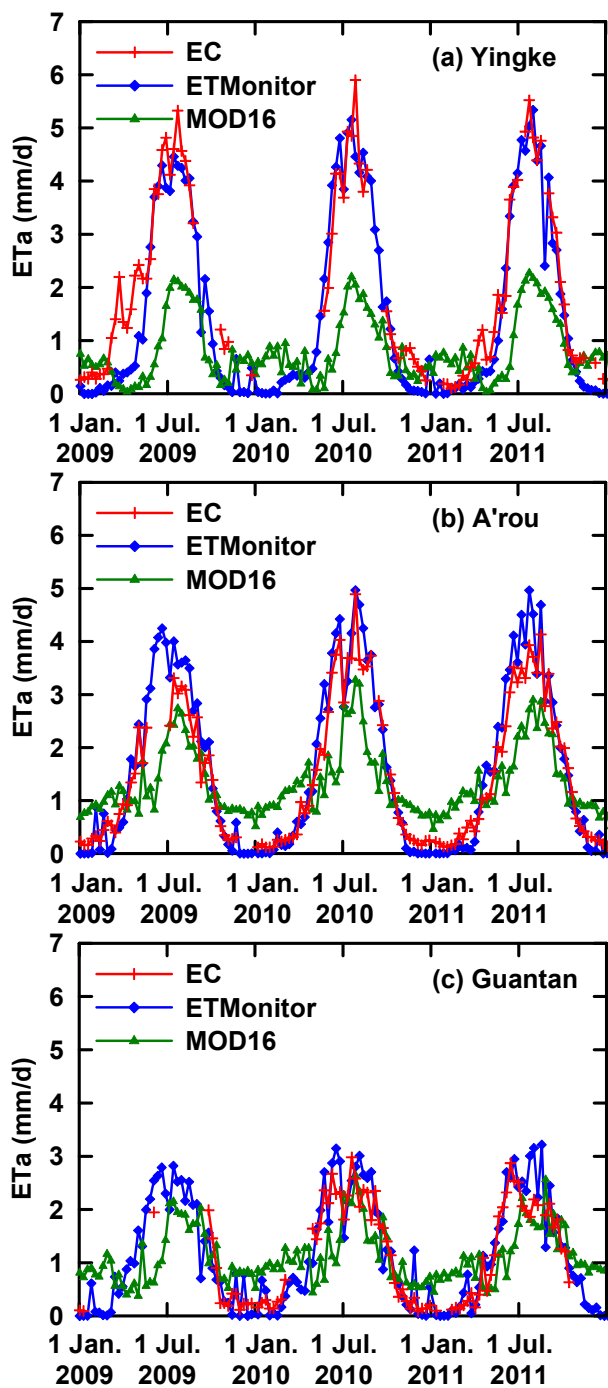


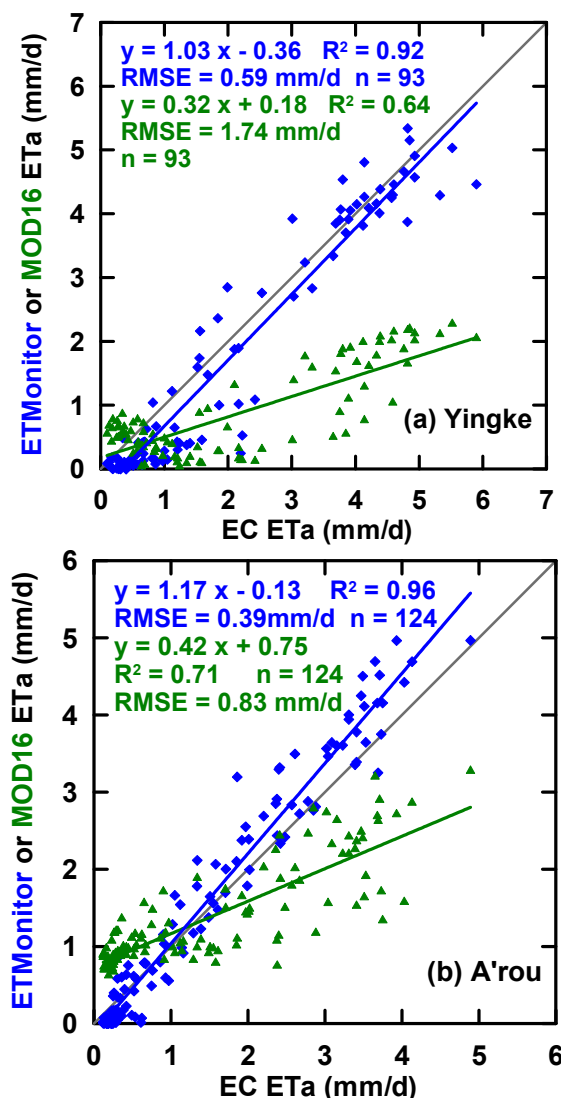
**Figure 5.** Three-year eight-day time series of ETMonitor, MOD16 and eddy covariance (EC) observed evapotranspiration (ET<sub>a</sub>) spanning 2009–2011 at the site of (a) Yingke (cropland), (b) A'rou (alpine meadow), and (c) Guantan (forest). Values shown are the eight-day means of ET<sub>a</sub> (mm/day).

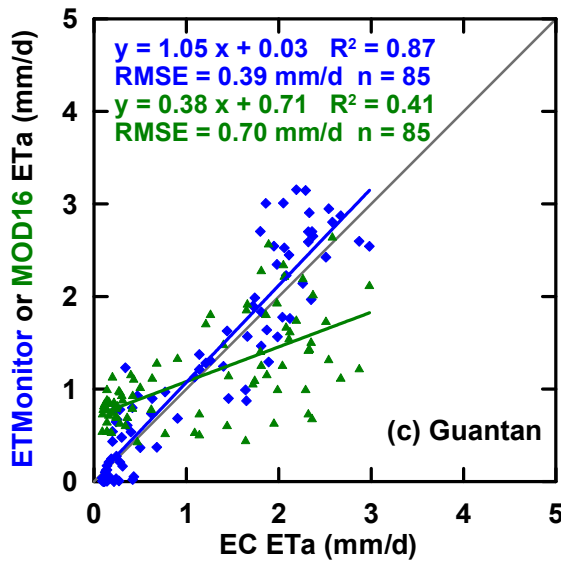
#### 5.1.2. Spatial Intercomparison with Precipitation and MOD16 ET<sub>a</sub>

To reveal the spatial pattern of the ET<sub>a</sub> from the ETMonitor in relation to the spatial patterns of the relevant environmental and biophysical variables, the annual ETMonitor ET<sub>a</sub> over the Heihe River basin in 2010 was compared with the TRMM precipitation and MOD16 ET<sub>a</sub>, respectively (Figure 7). The annual precipitation exhibits a distinguishable southeast to northwest decreasing gradient,

corresponding to the climate conditions and topographic altitudes (Figure 7a). The difference between precipitation and ETMonitor ETa indicates that precipitation is higher than ETMonitor ETa in the up reaches of the Heihe River basin due to the high precipitation and low-to-moderate temperatures (Figure 7b). Contrarily, for the oases in the middle and lower reaches, especially for the agriculturally dominated regions whose natural climate alone cannot sustain the current level of agriculture, ETa exceeds precipitation due to importing water by diverting surface water from the Heihe River and reservoirs, or by pumping groundwater, and the results of this comparison are consistent with the regional hydrologic cycle of the basin.

The annual MOD16 ETa in 2010 is about 400–600 mm/year in the up reaches, whereas much lower than 400 mm/year over the irrigated oases in the middle, and even lower (less than 100 mm/year) in the lower reaches of the basin (Figure 7c). Accordingly, the difference between MOD16 and ETMonitor ETa shows very large discrepancy between the up reaches and the middle and lower reaches of the basin (Figure 7d). The spatial intercomparison results between the MOD16 and the ETMonitor ETa indicate that MOD16 ETa is greatly overestimated in the semi-humid up reaches of the Heihe River basin, which agrees with the evaluation results obtained using a water balance method for the upper Yellow River and Yangtze River basins on the Tibetan Plateau [75].



**Figure 6.** *Cont.*

**Figure 6.** Scattering plots of the ETMonitor (blue diamonds) and MOD16 (green triangles) ETa against EC observations spanning 2009–2011 at the site of (a) Yingke (cropland), (b) A’rou (alpine meadow), and (c) Guantan (forest). Values shown are the eight-day means of ETa (mm/day).

### 5.2. Sensitivity Analysis

A sensitivity analysis was performed to explore the influence of the environmental and land surface biophysical parameters on the ETa estimates by the ETMonitor model. These parameters include the remote sensing based parameters, the meteorological forcing variables, and the static model parameters. The sensitivity  $S_p$  of ETa to a parameter  $p$  is defined as [76]:

$$S_p = \left| \frac{ET_{0.9r} - ET_{1.1r}}{ET_r} \right| \quad (28)$$

where  $ET_r$ ,  $ET_{0.9r}$ , and  $ET_{1.1r}$  are the ETa (soil evaporation and vegetation canopy transpiration) derived by the ETMonitor when the parameter  $p$  equals to its reference value  $p_r$ ,  $0.9p_r$ , and  $1.1p_r$ , respectively, and all other parameters are set to their reference values. The reference values of the remote sensing based parameters (*i.e.*, NDVI, albedo, and surface layer soil water content) and the meteorological forcing variables are taken as their mean values in the growing season (from May to September) at the Yingke site. The sensitivity results are listed in Table 2, which indicate that the model shows larger sensitivity to the NDVI and the surface layer soil water content among the remote sensing based parameters, to the downward radiation fluxes among the meteorological forcing data, and to the minimum stomatal resistance and the saturated soil water content among the static model parameters. These parameters/variables are the most critical data/parameters needed for further improvement and refinement. It should be noted that the ETMonitor shows much less sensitivity to the wind speed (which is used to calculate the aerodynamic resistance), this can be attributed to the presence of the aerodynamic resistance in both the numerator and in the denominator of the Penman–Monteith equation.

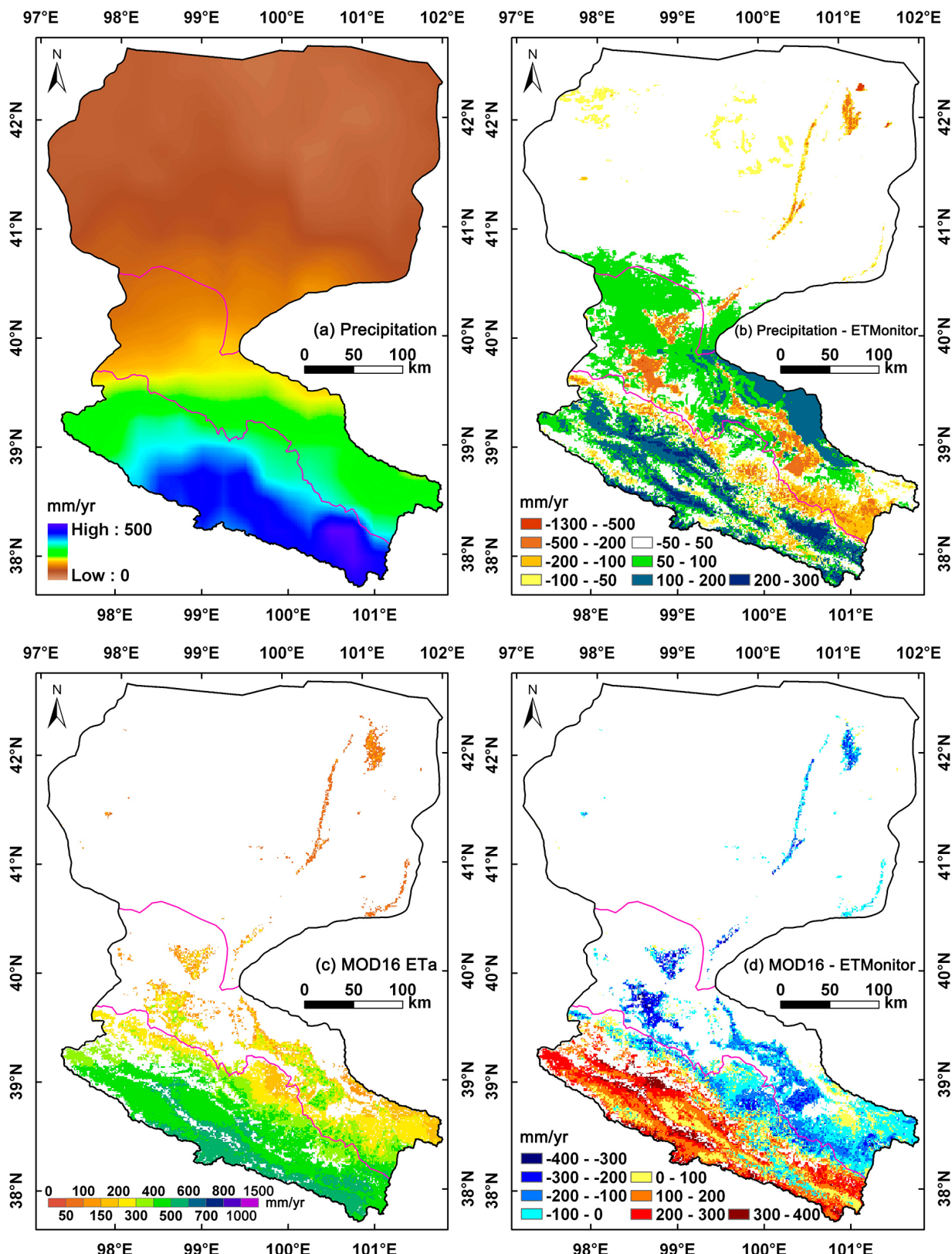


**Figure 7.** Spatial comparisons of the annual ETMonitor evapotranspiration (ETa) in 2010 with (a),(b) Tropical Rainfall Measuring Mission (TRMM) precipitation and (c),(d) MOD16 ETa in the Heihe River basin. In (c) and (d), the regions in white are sparsely vegetated and non-vegetated areas.

**Table 2.** Sensitivity of the ETMonitor to environmental and land surface biophysical parameters with  $\pm 10\%$  range of variation in the parameters from their reference values.

Parameter	Reference Value	$ET_r$ ( $\text{mm} \cdot \text{d}^{-1}$ )	$ET_{0.9r}$ ( $\text{mm} \cdot \text{d}^{-1}$ )	$ET_{1.1r}$ ( $\text{mm} \cdot \text{d}^{-1}$ )	Sensitivity
NDVI	NDVI (-)	0.66	2.914	3.964	0.295
Albedo	Albedo (-)	0.19	3.619	3.505	0.032
Surface layer soil water content	$\theta_g$ ( $\text{cm}^3 \cdot \text{cm}^{-3}$ )	0.12	3.373	3.748	0.105
Air temperature	$T_a$ ( $^\circ\text{C}$ )	21.3	3.365	3.662	0.084
Air pressure	$P$ (Pa)	84540	3.877	3.287	0.166
Specific humidity	$Q$ ( $\text{kg} \cdot \text{kg}^{-1}$ )	0.006	3.605	3.514	0.026
Wind speed	$u$ ( $\text{m} \cdot \text{s}^{-1}$ )	3	3.570	3.564	0.002
Downward short-wave radiation	$R_s$ ( $\text{W} \cdot \text{m}^{-2}$ )	293.8	3.193	3.932	0.207
Downward long-wave radiation	$R_l$ ( $\text{W} \cdot \text{m}^{-2}$ )	330.8	3.230	3.893	0.186
Minimum stomatal resistance	$r_{st,\min}$ ( $\text{s} \cdot \text{m}^{-1}$ )	180	3.744	3.398	0.097
Minimum soil surface resistance	$r_{ss,\min}$ ( $\text{s} \cdot \text{m}^{-1}$ )	50	3.601	3.528	0.021
Saturated soil water content	$\theta_{sat}$ ( $\text{cm}^3 \cdot \text{cm}^{-3}$ )	0.5	3.768	3.390	0.106
Solar radiation factor	$k_{Rs}$ ( $\text{W} \cdot \text{m}^{-2}$ )	500	3.693	3.440	0.071
Optimum air temperature	$T_{opt}$ ( $^\circ\text{C}$ )	25	3.595	3.510	0.024
Vapor pressure deficit factor	$k_{VPD}$ ( $\text{hPa}^{-1}$ )	0.023	3.671	3.446	0.063
Tenacity factor	$K_{sf}$ (-)	1.5	3.402	3.709	0.086

### 5.3. ET<sub>a</sub> Spatial and Temporal Variations in the Heihe River Basin

The multi-year average of annual precipitation for the entire Heihe River basin is 121.9 mm/year. In 2009–2011, the annual precipitation is, respectively, 124.1, 148.5, and 131.0 mm/year, so 2010 is a typical wet year and the estimated ET<sub>a</sub> of 2010 was primarily used to analyze the spatial and temporal variations of ET<sub>a</sub> in the Heihe River basin.

#### 5.3.1. Characteristics of ET<sub>a</sub> in the Upstream, Middle Stream and Downstream Areas

The spatial patterns of the annual ET<sub>a</sub> spanning 2009–2011 in the Heihe River basin are presented in Figure 8. As expected, the estimated ET<sub>a</sub> shows consistent patterns with the landscapes over the upstream, middle stream and downstream regions:

(1) In the up reaches of the Heihe River basin, the annual ET<sub>a</sub> is about 300–600 mm/year in the east part of the up reaches due to the higher vegetation coverage and more humid climate. The annual ET<sub>a</sub> is less than 300 mm/year in the cold and arid west part of the up reaches. For the regions covered by permanent snow and glaciers in the mountain cryosphere, the magnitude of annual sublimation is about 200–300 mm/year. The seasonal snow is distributed in the mountain cryosphere of the east part of the up reaches, and the snow has completely melted away in summer, resulting that the annual sublimation is much lower than that of the permanent snow and glaciers in the west part of the up reaches.

(2) In the middle reaches, the typical landscapes include irrigated oasis, riparian ecosystem, wetland, and desert. The annual ET<sub>a</sub> is more than 500 mm/year in the artificial oasis due to irrigation. The major crops are maize, spring wheat and vegetables, which are irrigated about five times during the growing

season, and the irrigation quota of the Zhangye Oasis is about  $6000 \text{ m}^3/\text{hm}^2$  per year (6 ML/ha per year, or 600 mm/year). In the surrounding barren regions the annual ET<sub>a</sub> is less than 200 mm/year.

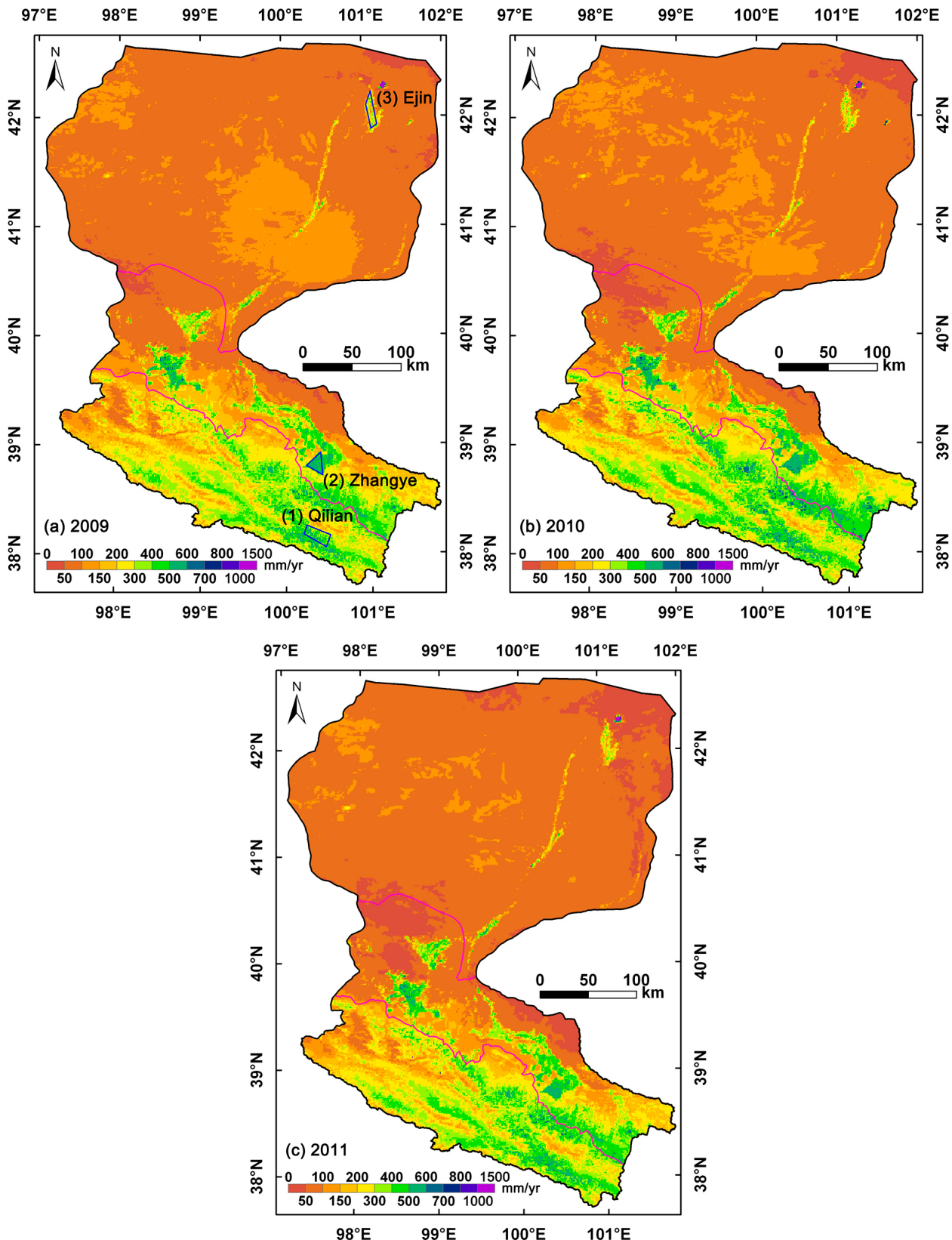


**Figure 8.** Spatial patterns of the annual ET<sub>a</sub> spanning 2009–2011 (a–c) in the Heihe River basin with the maximum ET<sub>a</sub> of 1400 mm/year at the terminal lake.

(3) In the lower reaches, the annual ETa is about 100–400 mm/year over the river greenbelt and Ejin Oasis and less than 100 mm/year in the most desolate parts of the Gobi desert. The maximum ETa of 1400 mm/year is observed at the terminal East Juyanhai Lake, which has not been dried up since 2004 due to the transfer of water from the Heihe River. The Tian'e Lake, which is located in the southeast of the Ejin Oasis, is seasonally covered by shallow water with the annual ETa of about 700 mm/year in 2010.

The spatial average of the annual ETa in 2009, 2010, and 2011 for the entire Heihe River basin is 140.3, 146.5, and 131.5 mm/year, respectively, which are higher than the multi-year average of 123.3 mm/year derived by the catchment water balance approach [77]. For the catchment water balance approach in [77], the annual evapotranspiration integrated over the entire inland Heihe River basin was estimated as the sum of total annual precipitation, total annual overdraft of groundwater and total annual runoff from the glaciers.

The histograms of the annual ETa in the upstream (Qilian), middle stream (Zhangye) and downstream (Ejin) regions indicated by rectangles/triangles in Figure 8a are presented in Figure 9. There are three peak values around 300–350, 400–450, and 500–550 mm/year in the upstream Qilian area (Figure 9a), indicating the strong spatial heterogeneity due to the rolling topography. Whereas in the middle stream and downstream regions, the annual ETa exhibits some homogeneity in the artificial oasis with respect to the upstream area. The annual ETa in 2010 is obviously higher than that in 2009 and 2011 as shown in Figure 9. The annual ETa of the Ejin Oasis is much lower and the histograms in different years are also very similar.

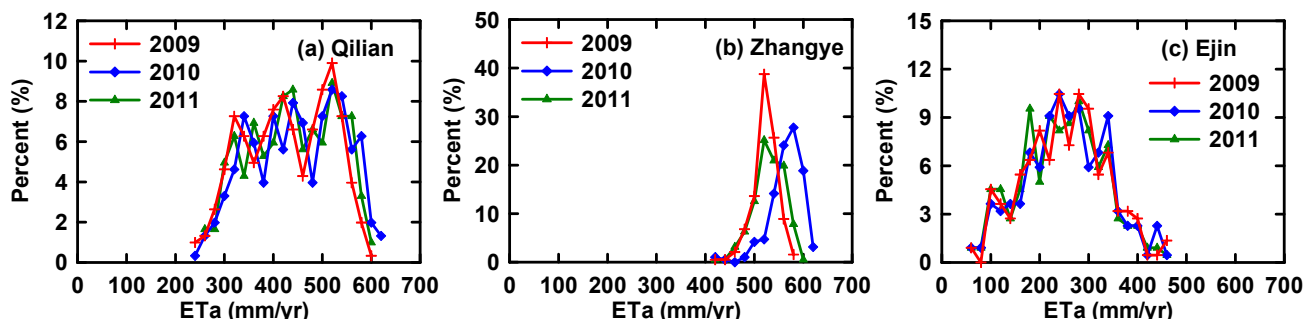


**Figure 9.** Histograms of the annual ETa in the (a) upstream (Qilian), (b) middle stream (Zhangye), and (c) downstream (Ejin) regions illustrated in Figure 8a.

### 5.3.2. Land Cover Dependence and Temporal Variation

Evapotranspiration varies substantially between different land cover types in the Heihe River basin, which is demonstrated in Figure 10. The ETa of spruce forest in 2010 is the lowest among the four vegetation types shown in Figure 10a. The potato is mainly distributed near the Jiuquan Oasis and planted in mid-April, whereas the maize is mainly distributed near the Zhangye Oasis and planted in mid-May. The ETa of potato reaches a maximum at around Julian Day of Year (DOY) 169, which is earlier than maize (around DOY 193) and alpine meadow (around DOY 201). At DOY 177, the decrease of ETa is due to the cloudiness, especially for the alpine meadow and spruce forest, which are distributed in the upstream Qilian Mountains of the Heihe River basin.

The sublimation of mountain glaciers distributed in the southwest of Jiuquan varies between 0 and 1.5 mm/day in different seasons of 2010, with the minimum recorded in the period DOY 177–209 due to the decrease of wind speed (Figure 10b). In winter, sublimation is the main kind of water loss over the frozen East Juyanhai Lake. With the increase of air temperature, the ETa of the East Juyanhai Lake gradually increases and reaches a maximum of about 8 mm/day due to the extremely arid climate. The ETa of the Gobi desert in the downstream area of the basin is much less than the ETa of the other land cover types in the Heihe River basin, with the values less than 1 mm/day throughout the year.

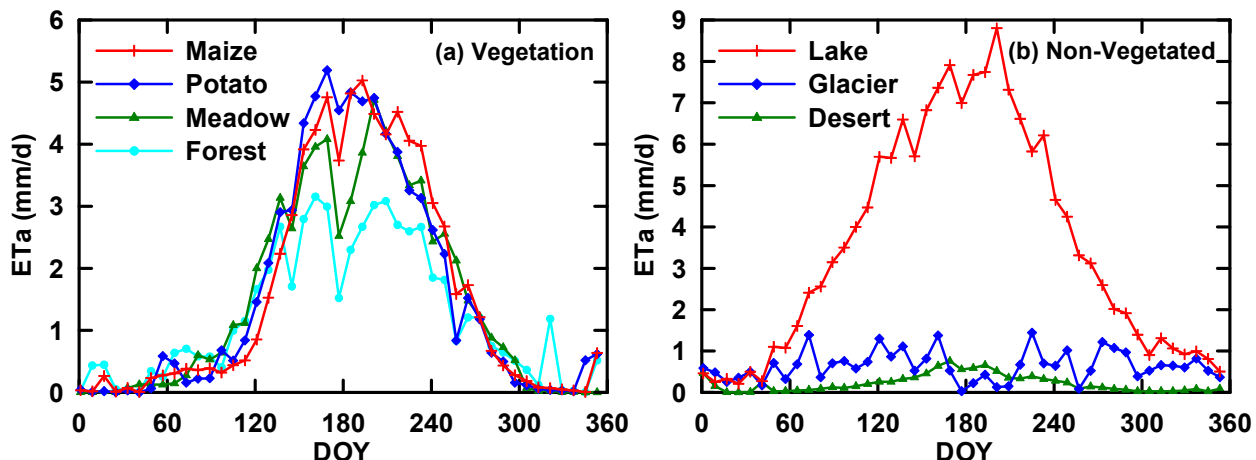


**Figure 10.** Seasonal variations of the ETa for (a) different vegetation types and (b) non-vegetated classes in 2010. Values shown are the eight-day means of ETa (mm/day).

The annual ETa of different land cover types in the Heihe River basin is demonstrated in Figure 11. The mean annual ETa of the croplands (maize and potato) is 550–600 mm/year in 2009–2011, a little higher than that of the alpine meadow (550 mm/year) and of the spruce forest (400–450 mm/year). Figure 11 also shows that the highest mean annual ETa values (1200–1400 mm/year) in the Heihe River basin occurred over the East Juyanhai Lake, and the lowest ETa values (less than 100 mm/year) was in the Gobi desert. Besides, the mean sublimation of mountain glaciers is about 200–250 mm/year in 2009–2011.

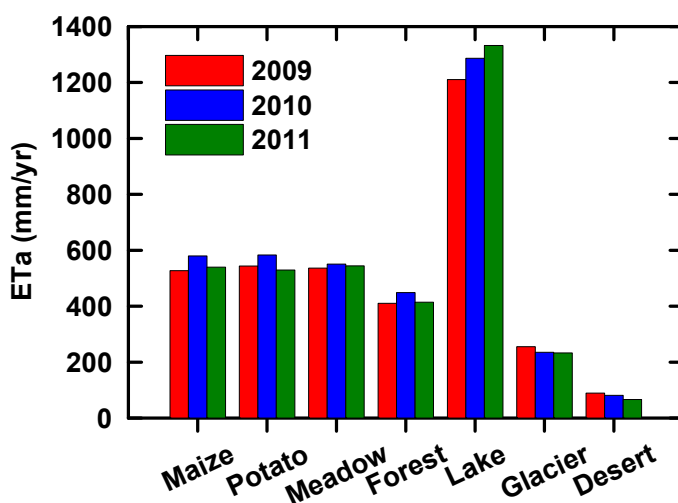


**Figure 11.** The annual ETa of different land cover types spanning 2009–2011 in the Heihe River basin.

## 6. Discussion

ETMonitor is developed based on the concept of the Shuttleworth–Wallace dual-source model with some resistance-based methods. The sensitivity analysis indicates that minimizing the sensitivity of the model to wind speed has significant advantages because the wind speed is not easily and accurately determined for heterogeneous landscapes over large scales. While the equations used in the ETMonitor model is physically robust enough, yet they can be solved without any iterative procedure. As such, the ETMonitor is easy to be implemented to generate daily time series of continental and global ET<sub>a</sub> datasets with a moderate spatial resolution (1 km).

The near-surface meteorological forcing data used in this study was derived based on the Weather Research and Forecasting model (WRF). With respect to data sparse regions, reanalysis meteorological products can be used due to the lack of spatially and temporally complete *in-situ* observations. The typically used reanalysis products include NCEP–NCAR reanalysis and Climate Forecast System Reanalysis (CFSR) from NCEP; Modern-Era Retrospective Analysis for Research and Applications (MERRA) and Global Land Data Assimilation System (GLDAS) from the Goddard Space Flight Center (GSFC); and 40-yr European Centre for Medium-Range Weather Forecasts (ECMWF) Re-Analysis (ERA-40) and ECMWF Interim Re-Analysis (ERA-Interim) from ECMWF. Decker *et al.* [78] evaluated these reanalysis products using flux tower observations, concluding that the ERA-Interim dataset is slightly better than all of the rest.

The Qilian Mountain area has a steep topography, and the elevation, aspect and slope are the main topographic factors that affect the distribution of precipitation, temperature, land cover/land use, and soil types in mountain areas indirectly. Topographic influences (elevation, aspect and slope) are important considerations to downscale the model input data in areas with high-localized relative relief [79,80]. As stated in Section 5.1.1, the accuracy of the ET<sub>a</sub> estimates for the cropland and grassland are higher than that of the forests. The mountain climate has a strong spatial heterogeneity over the mountain area, which cannot be fully captured by the downscaled meteorological forcing data. The complex canopies with short vegetation understories may also lead to the erroneous ET<sub>a</sub> estimates of the forests. The biases between the ET<sub>a</sub> estimates and the EC measurements can also arise from the inaccuracy of the EC measurements which have an uncertainty of about 10%–30% [19], especially for the areas with rolling topography. Besides, it should be noted that the following aspects need further investigations and studies:

(1) During different stages of the vegetation growing season from the initial, through development and mid-season, and to the late season, the minimum stomatal resistance  $r_{st,min}$  may vary substantially between the four distinct growth stages of various types of vegetation. In ETMonitor,  $r_{st,min}$  is taken as a single constant value for each vegetation type spanning the entire growing season, which needs to be improved based on the field observations in the Heihe River basin.

(2) The soil moisture data derived from passive microwave sensors, such as AMSR-E, Soil Moisture and Ocean Salinity (SMOS), and Fengyun-3 (FY-3) MicroWave Radiation Imager (MWRI) have a coarse spatial resolution (25 km), which is not sufficient for regional scale studies [73,74]. The accuracy and spatial resolution will improve in the near future [81,82]. The on-going National Aeronautics and Space Administration (NASA) Soil Moisture Active and Passive (SMAP) mission (launched on 31 January 2015) will provide more precise soil moisture data at a higher spatial resolution [83]. The spatial resolution of SMAP Level 3 soil moisture data product is 3 km (Radar),

36 km (Radiometer), and 9 km (Radar + Radiometer). The SMAP Level 4 product will provide a global surface and root zone soil moisture data set at a spatial resolution of 9 km. Besides, some downscaling methods to downscale the spatial resolution of passive microwave soil moisture data have achieved some developments [84], and a soil moisture product with a spatial resolution of 1 km will be generated by merging microwave remote sensing data and MODIS VI products. This is very useful to develop and improve the performance of ETa models based on soil moisture data.

(3) The spatial and temporal resolutions of the TRMM precipitation data used in this study is 0.25°/tri-hourly, which is also not sufficient for regional scale studies. The Global Precipitation Measurement (GPM) mission has been designed to provide more accurate/frequent observations of global precipitation using the GPM Core Observatory satellite (launched on 27 February 2014 by NASA-JAXA) with the Constellation Satellites (international partners' satellites with precipitation measurement capability). The 0.1°/30-minute global (90°N–90°S) precipitation data have been released in near real time (about 4 hours after observation) since March 2014 to present (available at <http://pmm.nasa.gov/data-access/downloads/gpm> (accessed on 15 January 2015)). Such data are very useful to improve the accuracy of the canopy interception estimates.

As stated in Section 5.1.1, the MOD16 ETa is underestimated in the growing season, especially for the irrigated artificial oasis located in a semi-arid climate. Such findings are in accordance with those obtained from previous studies over China [85,86], the conterminous United States [87], Brazil [88], South Africa [89], and Spain [90]. MOD16 ETa is not constrained explicitly by soil moisture and assumes that water availability can be captured by atmospheric VPD [91,92]. For soil evaporation estimation, the formulation of the soil moisture constraint in the MOD16 ETa algorithm does not include the stress factor for surface layer soil moisture, whereas the VPD and relative humidity are used as indicators of water stress. For canopy transpiration estimation, the formulation of canopy resistance in the MOD16 ETa algorithm is based on the VPD rather than the root-zone soil moisture. When the soil water content in the surface and root-zone layers are high, e.g., due to irrigation or thawing of frozen soil, the soil evaporation and canopy transpiration are underestimated due to the overestimation of water stress parameterized by the atmospheric VPD and relative humidity in the semi-arid middle reaches of the Heihe River basin.

## 7. Conclusions

We developed a remotely sensed ETa model (ETMonitor) to estimate the daily actual evapotranspiration of the Heihe River basin for the years 2009–2011 at a spatial resolution of 1 km. The estimated ETa was compared with the annual TRMM precipitation and the MOD16 ETa product, and was evaluated against *in-situ* measurements at the site of Yingke (cropland), A’rou (alpine meadow), and Guantan (forest), respectively. The evaluation and validation results demonstrate that the ETMonitor model performs better for alpine meadow (grassland) and cropland than for the forest, and achieves much higher accuracy compared with the MOD16 ETa. The soil moisture is a major factor contributing to ETa underestimation for cropland in spring, which needs to be improved both in the aspect of retrieval algorithm and downscaling.

The estimated ETa shows reasonable spatial and temporal patterns with respect to the diverse cold and arid landscapes in the Heihe River basin. The terminal lake surrounded by desert has the highest

ET<sub>a</sub> with the annual ET<sub>a</sub> of 1400 mm/year in 2010. The ET<sub>a</sub> of crops in the irrigated artificial oasis is much higher than the natural vegetation, e.g., alpine meadow and spruce forest. The seasonal variation of ET<sub>a</sub> for a specific crop variety is primarily determined by its phenology. The daily ET<sub>a</sub> is produced for all sky conditions, which is continuous and consistent at spatial and temporal scales and useful for integrated eco-hydrological studies and water resource management to improve the rational allocation of water resources with more efficiency, equity, and sustainability in the Heihe River basin. Registered users can access these data (2009–2011) through the Heihe Plan Science Data Center (<http://www.heihedata.org/>, doi:10.3972/heihe.114.2013.db (accessed on 15 January 2015)). Long-term series of ET<sub>a</sub> will be produced covering the years 2001–2015 at 1 km and daily resolutions, which will be used for the prediction and estimation of regional-scale surface runoff and groundwater, for the scheduling of field irrigations, and for the validation of the integrated water–ecosystem–economy model developed for the Heihe River basin [93].

## Acknowledgments

This work is supported by the National Natural Science Foundation of China (NSFC) (Grant no. 91425303) and the National Key Basic Research Program of China (Grant no. 2015CB953702). Eddy covariance flux tower sites are collected from Watershed Allied Telemetry Experimental Research (WATER) and provided by Cold and Arid Regions Sciences Data Center at Lanzhou, and we gratefully acknowledge the efforts of researchers at these sites.

## Author Contributions

Guangcheng Hu was responsible for the study and the write up of the manuscript with contributions for the model design, the parameterization, validation and article construction from Li Jia.

## Conflicts of Interest

The authors declare no conflict of interest.

## References

1. Nian, Y.Y.; Li, X.; Zhou, J.; Hu, X.L. Impact of land use change on water resource allocation in the middle reaches of the Heihe River Basin in northwestern China. *J. Arid Land* **2014**, *6*, 273–286.
2. Zeng, Z.; Liu, J.; Koeneman, P.H.; Zarate, E.; Hoekstra, A.Y. Assessing water footprint at river basin level: A case study for the Heihe River Basin in northwest China. *Hydrol. Earth Syst. Sci.* **2012**, *16*, 2771–2781.
3. Ge, Y.C.; Li, X.; Huang, C.L.; Nan, Z.T. A Decision Support System for irrigation water allocation along the middle reaches of the Heihe River Basin, Northwest China. *Environ. Model. Softw.* **2013**, *47*, 182–192.
4. Leuning, R.; Zhang, Y.Q.; Rajaud, A.; Cleugh, H.; Tu, K. A simple surface conductance model to estimate regional evaporation using MODIS leaf area index and the Penman–Monteith equation. *Water Resour. Res.* **2008**, doi:10.1029/2007WR006562.

5. Carlson, T.N.; Capehart, W.J.; Gillies, R.R. A new look at the simplified method for remote sensing of daily evapotranspiration. *Remote Sens. Environ.* **1995**, *54*, 161–167.
6. Wang, K.C.; Liang, S.L. An improved method for estimating global evapotranspiration based on satellite determination of surface net radiation, vegetation index, temperature, and soil moisture. *J. Hydrometeorol.* **2008**, *9*, 712–727.
7. Garcia, M.; Fernández, N.; Villagarcía, L.; Domingo, F.; Puigdefábregas, J.; Sandholt, I. Accuracy of the Temperature-Vegetation Dryness Index using MODIS under water-limited vs. energy-limited evapotranspiration conditions. *Remote Sens. Environ.* **2014**, *149*, 100–117.
8. Jiang, L.; Islam, S. A methodology for estimation of surface evapotranspiration over large areas using remote sensing observations. *Geophys. Res. Lett.* **1999**, *26*, 2773–2776.
9. Tang, R.L.; Li, Z.L.; Tang, B.H. An application of the Ts–VI triangle method with enhanced edges determination for evapotranspiration estimation from MODIS data in arid and semi-arid regions: Implementation and validation. *Remote Sens. Environ.* **2010**, *114*, 540–551.
10. Bastiaanssen, W.G.M.; Menenti, M.; Feddes, R.A.; Holtslag, A.A.M. A remote sensing surface energy balance algorithm for land (SEBAL): 1. Formulation. *J. Hydrol.* **1998**, *212*, 198–212.
11. Jia, L.; Su, Z.; van den Hurk, B.; Menenti, M.; Moene, A.; De Bruin, H.A.R.; Yrisarry, J.J.B.; Ibanez, M.; Cuesta, A. Estimation of sensible heat flux using the Surface Energy Balance System (SEBS) and ATSR measurements. *Phys. Chem. Earth* **2003**, *28*, 75–88.
12. Kustas, W.P.; Norman, J.M. Evaluation of soil and vegetation heat flux predictions using a simple two-source model with radiometric temperatures for partial canopy cover. *Agric. For. Meteorol.* **1999**, *94*, 13–29.
13. Norman, J.M.; Kustas, W.P.; Humes, K.S. Source approach for estimating soil and vegetation energy fluxes in observations of directional radiometric surface temperature. *Agric. For. Meteorol.* **1995**, *77*, 263–293.
14. Su, Z. The Surface Energy Balance System (SEBS) for estimation of turbulent heat fluxes. *Hydrol. Earth Syst. Sci.* **2002**, *6*, 85–99.
15. Bastiaanssen, W.G.M.; Cheema, M.J.M.; Immerzeel, W.W.; Miltenburg, I.J.; Pelgrum, H. Surface energy balance and actual evapotranspiration of the transboundary Indus Basin estimated from satellite measurements and the ETLook model. *Water Resour. Res.* **2012**, doi:10.1029/2011WR010482.
16. Cleugh, H.A.; Leuning, R.; Mu, Q.; Running, S.W. Regional evaporation estimates from flux tower and MODIS satellite data. *Remote Sens. Environ.* **2007**, *106*, 285–304.
17. Fisher, J.B.; Tu, K.P.; Baldocchi, D.D. Global estimates of the land atmosphere water flux based on monthly AVHRR and ISLSCP-II data, validated at FLUXNET sites. *Remote Sens. Environ.* **2008**, *112*, 901–919.
18. Mu, Q.Z.; Heinsch, F.A.; Zhao, M.S.; Running, S.W. Development of a global evapotranspiration algorithm based on MODIS and global meteorology data. *Remote Sens. Environ.* **2007**, *111*, 519–536.
19. Mu, Q.Z.; Zhao, M.S.; Running, S.W. Improvements to a MODIS global terrestrial evapotranspiration algorithm. *Remote Sens. Environ.* **2011**, *115*, 1781–1800.
20. Courault, D.; Seguin, B.; Olioso, A. Review on estimation of evapotranspiration from remote sensing data: From empirical to numerical modeling approaches. *Irrig. Drain. Syst.* **2005**, *19*, 223–249.

21. Kalma, J.D.; McVicar, T.R.; McCabe, M.F. Estimating land surface evaporation: A review of methods using remotely sensed surface temperature data. *Surv. Geophys.* **2008**, *29*, 421–469.
22. Li, Z.L.; Tang, R.L.; Wan, Z.; Bi, Y.; Zhou, C.; Tang, B.H.; Yan, G.J.; Zhang, X. A review of current methodologies for regional evapotranspiration estimation from remotely sensed data. *Sensors* **2009**, *9*, 3801–3853.
23. Li, S.B.; Zhao, W.Z. Satellite-based actual evapotranspiration estimation in the middle reach of the Heihe River Basin using the SEBAL method. *Hydrol. Process.* **2010**, *24*, 3337–3344.
24. Yang, Y.M.; Su, H.B.; Zhang, R.H.; Tian, J.; Yang, S.Q. Estimation of regional evapotranspiration based on remote sensing: Case study in the Heihe River Basin. *J. Appl. Remote Sens.* **2012**, doi:10.11117/1.JRS.6.061701.
25. Li, Z.L.; Tang, B.H.; Wu, H.; Ren, H.Z.; Yan, G.J.; Wan, Z.M.; Trigo, I.F.; Sobrino, J.A. Satellite-derived land surface temperature: Current status and perspectives. *Remote Sens. Environ.* **2013**, *131*, 14–37.
26. Ghilain, N.; Arboleda, A.; Sepulcre-Canto, G.; Batelaan, O.; Ardo, J.; Gellens-Meulenberghs, F. Improving evapotranspiration in a land surface model using biophysical variables derived from MSG/SEVIRI satellite. *Hydrol. Earth Syst. Sci.* **2012**, *16*, 2567–2583.
27. Monteith, J.L. Evaporation and environment. In *The State and Movement of Water in Living Organisms. Symposium of the Society of Experimental Biology*; Fogg, G.E., Ed.; Society of Experimental Biology, Cambridge University Press: Swansea, UK, 1965; Volume 19, pp. 205–234.
28. Liang, X.; Lettenmaier, D.P.; Wood, E.F.; Burges, S.J. A simple hydrologically based model of land surface water and energy fluxes for general circulation models. *J. Geophys. Res.* **1994**, *99*, 14415–14428.
29. Sellers, P.J.; Randall, D.A.; Collatz, G.J.; Berry, J.A.; Field, C.B.; Dazlich, D.A.; Zhang, C.; Collelo, G.D.; Bounoua, L. A revised land surface parameterization (SiB2) for atmospheric GCMs. Part I: Model formulation. *J. Clim.* **1996**, *9*, 676–705.
30. Shuttleworth, W.J.; Wallace, J.S. Evaporation from sparse crops—An energy combination theory. *Q. J. R. Meteorol. Soc.* **1985**, *111*, 839–855.
31. Anadranistakis, M.; Liakatas, A.; Kerkides, P.; Rizosb, S.; Gavanosisb, J.; Poulovassilis, A. Crop water requirements model tested for crops grown in Greece. *Agric. Water Manag.* **2000**, *45*, 297–316.
32. Shaw, R.H.; Pereira, A.R. Aerodynamic roughness of a plant canopy: A numerical experiment. *Agric. Meteorol.* **1982**, *26*, 51–65.
33. Gutman, G.; Ignatov, V. The derivation of the green vegetation fraction from NOAA/AVHRR data for use in numerical weather prediction models. *Int. J. Remote Sens.* **1998**, *19*, 1533–1543.
34. Camillo, P.J.; Gurney, R.J. A resistance parameter for bare-soil evaporation models. *Soil Sci.* **1986**, *141*, 95–105.
35. Clapp, R.B.; Hornberger, G.M. Empirical equations for some soil hydraulic properties. *Water Resour. Res.* **1978**, *14*, 601–604.
36. Dolman, A.J. A multiple-source land surface energy balance model for use in general circulation models. *Agric. For. Meteorol.* **1993**, *65*, 21–45.
37. Van Genuchten, M.T. A closed-form equation for predicting the hydraulic conductivity of unsaturated soils. *Soil Sci. Soc. Am. J.* **1980**, *44*, 892–898.

38. Avissar, R.; Avissar, P.; Mahrer, Y.; Bravdo, B.A. A model to simulate response of plant stomata to environmental conditions. *Agric. For. Meteorol.* **1985**, *34*, 21–29.
39. Jarvis, P.G. The interpretation of the variations in leaf water potential and stomatal conductance found in canopies in the field. *Philos. Trans. R. Soc. Lond. B* **1976**, *273*, 593–610.
40. Stewart, J.B. Modelling surface conductance of pine forest. *Agric. For. Meteorol.* **1988**, *43*, 19–35.
41. Mehrez, M.B.; Taconet, O.; Vidal-Madjar, D.; Valencogne, C. Estimation of stomatal resistance and canopy evaporation during the HAPEX–MOBILHY experiment. *Agric. For. Meteorol.* **1992**, *58*, 285–313.
42. Dickinson, R.E. Modelling evapotranspiration for three-dimensional global climate models. *Geophys. Monogr. Ser.* **1984**, *29*, 58–72.
43. Irannejad, P.; Shao, Y.P. Description and validation of the atmosphere–land–surface interaction scheme (ALYSIS) with HAPEX and Cabauw data. *Glob. Planet. Chang.* **1998**, *19*, 87–114.
44. Mo, X.G.; Liu, S.X.; Lin, Z.H.; Zhao, W.M. Simulating temporal and spatial variation of evapotranspiration over the Lushi basin. *J. Hydrol.* **2004**, *285*, 125–142.
45. Sellers, P.J.; Mintz, Y.; Sud, Y.C.; Dalcher, A. A simple biosphere model (SiB) for use within general circulation models. *J. Atmos. Sci.* **1986**, *43*, 505–531.
46. Noilhan, J.; Planton, S. A simple parameterization of land surface processes for meteorological models. *Mon. Weather Rev.* **1989**, *117*, 536–549.
47. Allen, R.G.; Pruitt, W.O.; Businger, J.A.; Fritsch, L.J.; Jensen, M.E.; Quinn, F.H. Evaporation and transpiration. In *Hydrology Handbook*, 2nd ed.; Task Committee on Hydrology Handbook of Management Group D of American Society of Civil Engineers (ASCE), Ed.; ASCE: New York, NY, USA, 1996; pp. 125–252.
48. Gash, J.H.C.; Lloyd, C.R.; Lachaud, G. Estimating sparse forest rainfall interception with an analytical model. *J. Hydrol.* **1995**, *170*, 79–86.
49. Van Dijk, A.I.J.M.; Bruijnzeel, L.A. Modelling rainfall interception by vegetation of variable density using an adapted analytical model. Part 1. Model description. *J. Hydrol.* **2001**, *247*, 230–238.
50. Cui, Y.K.; Jia, L. A modified Gash model for estimating rainfall interception loss of forest using remote sensing observations at regional scale. *Water* **2014**, *6*, 993–1012.
51. Cui, Y.K.; Jia, L.; Hu, G.C.; Zhou, J. Mapping of interception loss of vegetation in the Heihe River basin of China using remote sensing observations. *IEEE Geosci. Remote Sens. Lett.* **2015**, *12*, 23–27.
52. Kuzmin, P.P. On method for investigations of evaporation from the snow cover. *Trans. State Hydrol. Inst.* **1953**, *41*, 34–52. (In Russian)
53. Penman, H.L. Natural evaporation from open water, bare soil and grass. *Proc. R. Soc. A* **1948**, *193*, 120–145.
54. Liu, Q.; Wang, L.; Qu, Y.; Liu, N.; Liu, S.; Tang, H.; Liang, S. Preliminary evaluation of the long-term GLASS albedo product. *Int. J. Digit. Earth* **2013**, *6*, 69–95.
55. Jia, L.; Shang, H.; Hu, G.; Menenti, M. Phenological response of vegetation to upstream river flow in the Heihe River basin by time series analysis of MODIS data. *Hydrol. Earth Syst. Sci.* **2011**, *15*, 1047–1064.

56. Ran, Y.H.; Li, X.; Lu, L.; Li, Z.Y. Large-scale land cover mapping with the integration of multi-source information based on the Dempster–Shafer theory. *Int. J. Geogr. Inf. Sci.* **2012**, *26*, 169–191.
57. Zhong, B.; Ma, P.; Nie, A.H.; Yang, A.X.; Yao, Y.J.; Lv, W.B.; Zhang, H.; Liu, Q.H. Land cover mapping using time series HJ-1/CCD data. *Sci. China Earth Sci.* **2014**, *57*, 1790–1799.
58. Dai, Y.J.; Shangguan, W.; Duan, Q.Y.; Liu, B.; Fu, S.; Niu, G. Development of a China dataset of soil hydraulic parameters using pedotransfer functions for land surface modeling. *J. Hydrometeorol.* **2013**, *14*, 869–887.
59. Pan, X.D.; Li, X. Validation of WRF model on simulating forcing data for Heihe River Basin. *Sci. Cold Arid Region.* **2011**, *3*, 344–357.
60. Pan, X.D.; Li, X.; Shi, X.K.; Han, X.J.; Luo, L.H.; Wang, L.X. Dynamic downscaling of near-surface air temperature at the basin scale using WRF—A case study in the Heihe River Basin, China. *Front. Earth Sci.* **2012**, *6*, 314–323.
61. Gao, Y.C.; Long, D.; Li, Z.L. Estimation of daily actual evapotranspiration from remotely sensed data under complex terrain over the upper Chao river basin in North China. *Int. J. Remote Sens.* **2008**, *29*, 3295–3315.
62. Stahl, K.; Moore, R.D.; Floyer, J.A.; Asplin, M.G.; McKendry, I.G. Comparison of approaches for spatial interpolation of daily air temperature in a large region with complex topography and highly variable station density. *Agric. For. Meteorol.* **2006**, *139*, 224–236.
63. Li, X.; Li, X.W.; Li, Z.Y.; Ma, M.G.; Wang, J.; Xiao, Q.; Liu, Q.; Che, T.; Chen, E.X.; Yan, G.J.; *et al.* Watershed allied telemetry experimental research. *J. Geophys. Res.* **2009**, doi:10.1029/2008JD011590.
64. Li, X.; Cheng, G.D.; Liu, S.M.; Xiao, Q.; Ma, M.G.; Jin, R.; Che, T.; Liu, Q.H.; Wang, W.Z.; Qi, Y.; *et al.* Heihe Watershed Allied Telemetry Experimental Research (HiWATER) scientific objectives and experimental design. *Bull. Am. Meteorol. Soc.* **2013**, *94*, 1145–1160.
65. Liu, S.M.; Xu, Z.W.; Wang, W.Z.; Jia, Z.Z.; Zhu, M.J.; Bai, J.; Wang, J.M. A comparison of eddy-covariance and large aperture scintillometer measurements with respect to the energy balance closure problem. *Hydrol. Earth Syst. Sci.* **2011**, *15*, 1291–1306.
66. Blanken, P.D.; Black, T.A.; Neumann, H.H.; Den Hartog, G.; Yang, P.C.; Nesic, Z.; Staebler, R.; Chen, W.; Novak, M.D. Turbulent flux measurements above and below the overstory of a boreal aspen forest. *Bound. Layer Meteorol.* **1998**, *89*, 109–140.
67. Goulden, M.L.; Daube, B.C.; Fan, S.M.; Sutton, D.J.; Bazzaz, A.; Munger, J.W.; Wofsy, S.C. Physiological responses of a black spruce forest to weather. *J. Geophys. Res.* **1997**, *102*, 28987–28996.
68. Meyers, T.P.; Hollinger, S.E. An assessment of storage terms in the surface energy balance of maize and soybean. *Agric. For. Meteorol.* **2004**, *125*, 105–115.
69. Twine, T.E.; Kustas, W.P.; Norman, J.M.; Cook, D.R.; Houser, P.R.; Meyers, T.P.; Prueger, J.H.; Starks, P.J.; Wesely, M.L. Correcting eddy-covariance flux underestimates over a grassland. *Agric. For. Meteorol.* **2000**, *103*, 279–300.
70. Kustas, W.P.; Norman, J.M. Evaluating the effects of subpixel heterogeneity on pixel average fluxes. *Remote Sens. Environ.* **2000**, *74*, 327–342.

71. Kustas, W.P.; Li, F.; Jackson, T.J.; Prueger, J.H.; MacPherson, J.I.; Wolde, M. Effects of remote sensing pixel resolution on modeled energy flux variability of croplands in Iowa. *Remote Sens. Environ.* **2004**, *92*, 535–547.
72. Li, F.; Kustas, W.P.; Anderson, M.C.; Prueger, J.H.; Scott, R.L. Effect of remote sensing spatial resolution on interpreting tower-based flux observations. *Remote Sens. Environ.* **2008**, *112*, 337–349.
73. Chen, Y.Y.; Yang, K.; Qin, J.; Zhao, L.; Tang, W.J.; Han, M.L. Evaluation of AMSR-E retrievals and GLDAS simulations against observations of a soil moisture network on the central Tibetan Plateau. *J. Geophys. Res. Atmos.* **2013**, *118*, 4466–4475.
74. Yang, K.; Qin, J.; Zhao, L.; Chen, Y.Y.; Tang, W.J.; Han, M.L.; Lazhu; Chen, Z.Q.; Lv, N.; Ding, B.H.; et al. A multi-scale soil moisture and freeze-thaw monitoring network on the Third Pole. *Bull. Am. Meteorol. Soc.* **2013**, *94*, 1907–1916.
75. Xue, B.L.; Wang, L.; Li, X.P.; Yang, K.; Chen, D.L.; Sun, L.T. Evaluation of evapotranspiration estimates for two river basins on the Tibetan Plateau by a water balance method. *J. Hydrol.* **2013**, *492*, 290–297.
76. Zhan, X.; Kustas, W.P.; Humes, K.S. An intercomparison study on models of sensible heat flux over partial canopy surfaces with remotely sensed surface temperature. *Remote Sens. Environ.* **1996**, *58*, 242–256.
77. Cheng, G.D. *Integrated Management of the Water–Ecology–Economy System in the Heihe River Basin*; Science Press: Beijing, China, 2009. (In Chinese)
78. Decker, M.; Brunke, M.A.; Wang, Z.; Sakaguchi, K.; Zeng, X.B.; Bosilovich, M.G. Evaluation of the reanalysis products from GSFC, NCEP, and ECMWF using flux tower observations. *J. Clim.* **2012**, *25*, 1916–1944.
79. Liston, G.E.; Elder, K. A meteorological distribution system for high-resolution terrestrial modeling (MicroMet). *J. Hydrometeorol.* **2006**, *7*, 217–234.
80. McVicar, T.R.; Van Niel, T.G.; Li, L.T.; Hutchinson, M.F.; Mu, X.M.; Liu, Z.H. Spatially distributing monthly reference evapotranspiration and pan evaporation considering topographic influences. *J. Hydrol.* **2007**, *338*, 196–220.
81. Liu, Q.; Du, J.Y.; Shi, J.C.; Jiang, L.M. Analysis of spatial distribution and multi-year trend of the remotely sensed soil moisture on the Tibetan Plateau. *Sci. China Earth Sci.* **2013**, *56*, 2173–2185.
82. Shi, J.C.; Du, Y.; Du, J.Y.; Jiang, L.M.; Chai, L.N.; Mao, K.B.; Xu, P.; Ni, W.J.; Xiong, C.; Liu, Q.; et al. Progresses on microwave remote sensing of land surface parameters. *Sci. China Earth Sci.* **2012**, *55*, 1052–1078.
83. Das, N.N.; Entekhabi, D.; Njoku, E.G. An algorithm for merging SMAP radiometer and radar data for high-resolution soil-moisture retrieval. *IEEE Trans. Geosci. Remote Sens.* **2011**, *49*, 1504–1512.
84. Song, C.Y.; Jia, L.; Menenti, M. Retrieving high-resolution surface soil moisture by downscaling AMSR-E brightness temperature using MODIS LST and NDVI data. *IEEE J. Sel. Top. Appl. Earth Obs. Remote Sens.* **2014**, *7*, 935–942.
85. Liu, S.M.; Xu, Z.W.; Zhu, Z.L.; Jia, Z.Z.; Zhu, M.J. Measurements of evapotranspiration from eddy-covariance systems and large aperture scintillometers in the Hai River Basin, China. *J. Hydrol.* **2013**, *487*, 24–38.

86. Liu, Z.J.; Shao, Q.Q.; Liu, J.Y. The performances of MODIS-GPP and -ET products in China and their sensitivity to input data (FPAR/LAI). *Remote Sens.* **2015**, *7*, 135–152.
87. Velpuri, N.M.; Senay, G.B.; Singh, R.K.; Bohms, S.; Verdin, J.P. A comprehensive evaluation of two MODIS evapotranspiration products over the conterminous United States: Using point and gridded FLUXNET and water balance ET. *Remote Sens. Environ.* **2013**, *139*, 35–49.
88. Ruhoff, A.L.; Paz, A.R.; Aragao, L.E.O.C.; Mu, Q.; Malhi, Y.; Collischonn, W.; Rocha, H.R.; Running, S.W. Assessment of the MODIS global evapotranspiration algorithm using eddy covariance measurements and hydrological modelling in the Rio Grande basin. *Hydrol. Sci. J.* **2013**, *58*, 1–19.
89. Ramoelo, A.; Majozzi, N.; Mathieu, R.; Jovanovic, N.; Nickless, A.; Dzikiti, S. Validation of global evapotranspiration product (MOD16) using flux tower data in the African savanna, South Africa. *Remote Sens.* **2014**, *6*, 7406–7423.
90. Hu, G.C.; Jia, L.; Menenti, M. Comparison of MOD16 and LSA-SAF MSG evapotranspiration products over Europe for 2011. *Remote Sens. Environ.* **2015**, *156*, 510–526.
91. Garcia, M.; Sandholt, I.; Ceccato, P.; Ridler, M.; Mougin, E.; Kergoat, L.; Morillas, L.; Timouk, F.; Fensholt, R.; Domingo, F. Actual evapotranspiration in drylands derived from in-situ and satellite data: Assessing biophysical constraints. *Remote Sens. Environ.* **2013**, *131*, 103–118.
92. Vinukollu, R.K.; Wood, E.F.; Ferguson, C.R.; Fisher, J.B. Global estimates of evapotranspiration for climate studies using multi-sensor remote sensing data: Evaluation of three process-based approaches. *Remote Sens. Environ.* **2011**, *115*, 801–823.
93. Cheng, G.D.; Li, X.; Zhao, W.Z.; Xu, Z.M.; Feng, Q.; Xiao, S.C.; Xiao, H.L. Integrated study of the water–ecosystem–economy in the Heihe River Basin. *Natl. Sci. Rev.* **2014**, *1*, 413–428.

© 2015 by the authors; licensee MDPI, Basel, Switzerland. This article is an open access article distributed under the terms and conditions of the Creative Commons Attribution license (<http://creativecommons.org/licenses/by/4.0/>).